npj | clean water

Review article

Published in partnership with King Fahd University of Petroleum & Minerals

https://doi.org/10.1038/s41545-024-00425-3

Nanomaterial enhanced photoelectrocatalysis and photocatalysis for chemical oxygen demand sensing a comprehensive review

Luis D. Loor-Urgilés[1,2], Tabata N. Feijoó[2], Carlos A. Martínez-Huitle[2], Elisama Vieira dos Santos[2] & Patricio J. Espinoza-Montero[1]

Chemical oxygen demand-COD is essential for water pollution control and monitoring and is also used to validate wastewater treatment technologies. Conventional COD determination use of costly toxic inputs that do not align with Sustainable Development Goals 6. To address these environmental challenges, photocatalytic (PC)- and photoelectrocatalytic (PEC)-COD sensors have emerged as a solution. This comprehensive review examines PC-COD and PEC-COD sensors in terms of nanomaterials used and their properties, focusing on how multiple variables influence PC activity and sensor performance. Analytical principles and operational variables affecting performance in COD determination are discussed. Finally, a series of materials and conditions are proposed to improve the viability of PEC-COD sensors currently and in the future.

The management of organic load in industrial effluents plays a crucial role in environmental remediation[1–3]. Indeed, as mandated by the International Organization for Standardization (ISO) and the US Environmental Protection Agency, chemical oxygen demand (COD) concentrations in effluents must be lower than 150 mg L^{-1} before discharge into water bodies[4]. However, certain sectors, including the petroleum, carwash, agrochemical, and pharmaceutical industries, often produce effluents with COD concentrations ranging from 3000 to 6000 mg L^{-1}[5–11]. Given these high concentrations, it is imperative to control and monitor the total organic load in effluents to mitigate environmental pollution. This practice helps prevent negative impacts on aquatic ecosystems related to the accumulation of organic pollutants, such as species migration due to oxygen depletion, increased acidity, eutrophication, and the accumulation of endocrine – disrupting chemicals[12].

Conventional COD quantification methods are based on the oxidation of organic matter (OM) using strong oxidizing agents in an acidic medium, as permanganates ($E^0_{Mn^{7+}/Mn^{2+}} = 1.51V$) or dichromates ($E^0_{Cr^{6+}/Cr^{3+}} = 1.36V$) in sulfuric acid[2,13], and employ either volumetric or spectrophotometric techniques. However, they have several limitations, including i) the long analysis time required (2–5 h, which is often extended by systematic errors introduced by analyst interference); ii) errors related to the matrix effect; and iii) limited oxidizing capacity from costly (e.g., Ag_2SO_4), detection limits for each one of the apparatuses, and corrosive (e.g., H_2SO_4) reagents. Further, these reagents release toxic ions such as Hg^{2+}, Ag^+, and Ce^{4+} from electron scavengers, whose uncontrolled waste generates cross- and secondary contamination. Consequently, these methods are counterproductive, with low economic feasibility and viability[2,13–17]. Mainly, these issues contradict Sustainable Development Goals (SDGs) 6 and 14 and the green chemistry principles.

In contrast, COD sensors based on electrochemical[18] and/or electrochemical advanced oxidation processes (EAOPs), particularly photoelectrocatalytic (PEC) systems, offer a promising and sustainable alternative for precise and accurate organic detection in automated, short-duration analyses (1–5 min)[16,19–26]. PEC-COD sensors have gained popularity in recent years owing to their high mineralization efficiencies achieved through the photoelectrogeneration of hydroxyl radicals (•OH) from water, which are among the strongest green oxidants in nature with a half-life of about nanoseconds. The PEC principle behind these sensors involves developing and validating structurally functional nanomaterials that can absorb a broad-spectrum of visible light, enhancing their viability in line with SDG 7[12,27–38]. In practice, the working electrodes for PEC-COD sensors have been developed primarily using TiO_2[39–47], with variations in its morphology and structure achieved through alternative synthesis methods, doping with metals[48–51], or forming heterostructures with binary and ternary oxides[29,52,53], or other binary semiconductors such as nitrogen carbides[54] and cadmium sulfide[55].

[1]Escuela de Ciencias Químicas, Pontificia Universidad Católica del Ecuador, Quito, Ecuador. [2]Renewable Energies and Environmental Sustainability Research Group, Institute of Chemistry, Federal University of Rio Grande do Norte, Natal, Rio Grande do Norte, Brazil. e-mail: pespinoza646@puce.edu.ec

Then, this investigation in the existing literature provides a comprehensive review of research on PEC-COD sensors. It examines the nanomaterials used as working electrodes thus far and analyzes their photocatalytic (PC) performance, focusing on how morphological and structural manipulations through various synthesis and doping strategies affect their efficiency. It also explores the analytical principles of signal generation, as well as the optimization of the operational variables for both PC-COD and PEC-COD sensors. Lastly, it proposes a set of promising PC nanomaterials for future development in PEC-COD sensor research which have wide applicability as innovative environmental tools, and the materials science promotes the development of new energy advanced resources.

Nanomaterials employed in PEC-COD sensors

A key focus in EAOPs is optimizing the PC performance of semiconductors through controlled morphological and structural construction, achieved via nanomaterial synthesis and its modifications[12,56–58]. Research is thus centered on fabricating and validating novel materials with effective oxidation capabilities, stability, and low cost, ensuring reproducible and scalable results[59].

PC activity

PC and PEC processes primarily depend on the efficiency of photogenerated charge transfer and the degree of separation of the electron-hole recombination. Specifically, the kinetics of photoinduced charge transfer (k) from the valence band to the conduction band must be much higher than the kinetics of the electron-hole pair recombination, ($k_{(e^-_{VB}\rightarrow h^+_{CB})} \gg k_{(e^-_{CB}\rightarrow h^+_{VB})}$) [23,33,57,60–66]. Several strategies can optimize this behavior in quantum confinement, including efficient "charge extraction" by an external electric field in PC processes (PEC method) and modifying charge transfer mechanisms through material doping[30,57,61–64,67]. At the macro level, this translates to the precise manipulation and control of nanomaterial synthesis methodologies, considering the type and nature of the conductive substrate and the conditions of precursor preparation, deposition, and calcination, as summarized in Table 1.

TiO_2 in PEC-COD sensors

Over 80% of PEC-COD sensors employ TiO_2 semiconductors as working electrodes. These materials to COD sensors were primarily developed by Li et al.[15], Wang et al.[53], and Zhang et al.[68]. These research groups have utilized TiO_2 in both anatase and rutile phases, as well as their mixtures. The preference for TiO_2 stems from these phases' beneficial PC characteristics, which have established it as a benchmark in EAOPs. The effectiveness of TiO_2 is attributed to several key factors, including the morphology (Fig. 1), energy edge depth on the valence band, oxygen vacancy defects, and the arrangement of tetragonal structure holes on the surface. These features significantly enhance oxidation processes by promoting the high mobility of photoinduced charge carriers and are currently being actively studied[28,69].

Rutile and anatase phases of TiO_2 have tetragonal structures with octahedral geometry, where each titanium atom coordinates with six oxygen atoms per unit cell within the crystal lattice (Fig. 2a); however, their properties slightly differ in terms of octahedral distortion[56,69,70]. These phases are thermodynamically modifiable through variations in calcination treatments, such as temperature range and ramp. For instance, single-crystalline TiO_2-anatase nanofunctionals can be achieved at average temperatures of 400 °C[28,42], while rutile-phase TiO_2 is formed at about 700 °C[40,53,69].

Similarly, controlling the material's morphology and homogeneity can enhance conductivity, photoinduced electronic transitions, and particle size by increasing the contact surface area. Studies have used various strategies to develop single-dimensional TiO_2 (1D-TiO_2) nanostructures, as nanorods and nanotubes; among these, TiO_2 nanotubes (TNTs) are the most frequently used as working electrodes for PEC-COD sensors[40,68,71]. For instance, highly ordered TNTs were arranged (see Fig. 1a, b, and d) using electrochemical anodization in fluoride and citrate electrolytes under different experimental conditions (Table 1)[72]. In another example, 1D-TiO_2 amorphous spheres were obtained via hydrolysis of a titanium alkoxide precursor using the sol-gel method, followed by deposition on a conductive substrate like boron-doped diamond (BDD) (see Fig. 1c and Table 1)[43]. TNTs have also been generated through the electrochemical anodization of titanium metal. The use of citrate, diol, or fluoride electrolytes at a pH of 4.0 has been found to significantly contribute to the growth of ordered, long- and small-diameter nanotubes, which can be further controlled by adjusting the applied potential and anodization time, as shown in Table 1[37,49,54,55,73].

Dimensional optimization of TNTs is exemplified by comparing the work of Zhang et al.[74], and Liang et al.[51]. The former applied 20 V for 5 min, producing nanotubes with an inner diameter of 100 nm and a length of 350 nm (Fig. 1a and b). A decade later, the latter applied 60 V for 10 min, achieving vertically ordered nanotubes with an inner diameter of 65 nm and a length of 3 μm under the same calcination conditions (Fig. 1d).

TiO_2 nanorods (TNRs) are typically prepared using hydrothermal synthesis, a widely adopted method for achieving their crystalline structure[28,42,53,75] (Table 1). Both hydrothermal and solvothermal methods promote nanorod formation by facilitating the diffusion of titanium cations to the oxide surface, where their d-orbitals coordinate with n-electrons photoinduced from heteroatoms originating from either amine or carboxylic groups[17,40]. Zu et al.[28] synthetized rutile-TNRs (RTNRs) using the hydrothermal method, followed by a hydrogenated process (H-RTNRs) and further modified the surface to create an anatase-branched/hydrogenated rutile-TiO_2 nanorod photoelectrode (AB@H-RTNR). Figure 1g–i shows the morphological changes for each modification carried out by Zu et al.[28]: the hydrogenation and phase coupling affected charge distribution channels, increasing the photocurrent density at least threefold from RTNR to AB@H-RTNR and decreasing the energetic depth of the valence band density states during each modification step (Fig. 2b). Indeed, the valence band potential (E_{VB}) decreased from 1.69 eV for RTNR to 0.69 eV to AB@H-RTNR, and consequently lowering the band gap potential (E_{BG}) from 3.20 eV to 2.46 eV (Fig. 2c), thereby improving photoinduced electron transfer.

The PEC performance of TNT-based working electrodes has also been improved by surface hydrogenation[28,41,42]. This process generates oxygen vacancies in the crystal lattice by introducing hydrogen, which acts as surface charge density donors, thereby improving the electrical conductivity of TNTs. Consequently, less energetic wavelengths are required for the PC processes to occur[28,41,42]. Similarly, Mu et al.[39] synthesized TiO_2 nanofibers (TNFs) under hydrothermal conditions in an alkaline medium (see Fig. 1e), known as "template-free" synthesis. Ion exchange and titanium oxidation lead to the formation of anatase TNFs. Unlike the other nanostructures shown in Fig. 1, the long TNFs provide a larger contact area, resulting in higher PC efficiency, as evidenced by the molecular interaction scheme for OM on TiO_2 nanoparticles and TNFs in Fig. 1e.

TiO_2 nanopores (TNPs) with a uniform structure, as shown in Fig. 1, represent another innovative morphological approach[68]. These nanopores are produced through the electrochemical reduction of TNPs. This method enhances capacitance and increases delta photocurrent density by approximately 20 mA cm^{-2} compared to photocurrents generated from non-reduced TNPs produced via electrochemical anodization (Fig. 2f).

Doped-TNTs and other nanomaterials in PEC-COD sensors

Nanomaterial doping is another strategy for improving the PEC performance of semiconductors. This approach produces composites that promote charge distribution by increasing their density of states (DOS) at specific energetic band-edge positions[65]. Most of the dopings applied as working electrodes for PEC-COD-sensors involve modified TNTs with metals, metal oxides, and ternary oxides[48,50,51,57]. For instance, TNTs modified with conductive nanomaterials such as gold, platinum, and tellurium (AuNPs, PtNPs, and TeNPs, respectively) form a dielectric barrier known as a "Schottky contact". This barrier acts as an "electron trap," extending the photoinduced charged channels and facilitating more complex charge carrier transfer mechanisms (CTMs) between AuNPs, PtNPs, TeNPs with TNTs. The morphological modification of the TNTs can be seen under these conditions can be observed in Fig. 3a and is detailed in Table 1[37,48,51,77].

One previous study[52] developed a PEC-COD sensor by electrodepositing Cu_2O ($E_{BG\,Cu_2O} = 2.0eV$) on TNTs, as shown in Fig. 3b,

Table 1 | Experimental conditions for the preparation of working electrodes used in PEC-COD sensors

WE *Structure*	Reagents	Experimental conditions	Dimensions (nm)	Ref
TiO_2/ITO *Anatase amorphous*	P: Ti(i-PrO)$_4$ E: EtOH	ITO pretreatment, hydrolysis: [TiO_2] = 60 g L^{-1}, dip-coating, calcination at 450 °C for 30 min.	8 –10 (Th = 1.0 µm)	44,45,90,91
		ITO pretreatment, hydrolysis: [TiO_2] = 60 g L^{-1}, dip-coating, calcination at 700 °C for 3 h.	500	72
TNTs/Ti *Anatase*	P: Ti(i-PrO)$_4$ E: EtOH, polyethylene glycol	Titanium pretreatment, hydrolysis, dip-coating, laser treatment: Φ_{beam} = 1.5 mm, E_{laser} = 500000 mW for 30 min, calcination: T = 450 °C for 3 h.	30	46,47
	E: HF, $NaHSO_4$, Na_2-Citrate, NaOH.	Electrochemical anodization: E_{bias} = 20 V for 5 min at pH 4.0, calcination at 450 °C for 3 h.	Φ = 100, L = 350	17,74
	E: Ethylene glycol, NH_4F.	Electrochemical anodization: E_{bias} = 25 V for 2 h at υ = 500 mV s^{-1}, calcination at 700 °C for 1 h at υ = 5 °C min^{-1}, and hydrogenation at 450 °C for 2 h.	Φ = 100	41
TNPs/Ti *Anatase*	E: Ethylene glycol, NH_4F, H_2SO_4	Electrochemical anodization: E_{bias} = 50 V for 5, 2, 0.25 h, electrochemical reduction: j = −5 mA cm^{-2} for 10 min under Ar-bubbled, calcination at 450 °C for 3 h.	$\Phi_{outer\ TNPs}$ ca.150. $\Phi_{porous\ TNPs}$ ca. 50.	68
TNFs/Ti *Anatase*	E: NaOH, HNO_3	Hydrothermal synthesis, chemical oxidation, and calcination at 500 °C for 3 h.	Φ = 20	39
TiO_2/FTO *Anatase*	P: Ti(i-PrO)$_4$ E: CF_3-AcOH.	FTO pretreatment, peptization-hydrothermal synthesis, dip-coating, calcination at 500 °C for 4 h, # layers = 15.	3.6 ($Th_{bilayer}$ = 49 nm)	40
TNRs/FTO *Anatase*		Hydrolysis, hydrothermal synthesis at 150 °C for 8 h, calcination at 450 °C for 2 h.	Φ_{TNTs} = 100	41
H-TNRs/FTO *Rutile*		Hydrothermal synthesis: T = 170 °C for 9 h, Ar:H_2 flux = 80:20 mL min^{-1}, calcination: T = 350 °C for 1 h at υ = 5 °C min^{-1}.	$\Phi_{H\text{-}TNR}$ = 200, $L_{H\text{-}TNRs}$ = 2000	42
BDD *Diamond*	P: CH_4/H_2, B_2H_6	HF-CVD: C_{Borane} = 10 mg L^{-1}, and deposition for 2 h.	500–1500	84
TiO_2/BDD *Anatase and rutile mixed-phased*	P: $(ButO)_4Ti$ E: 2-PrOH	BDD pretreatment, hydrothermal synthesis: T = 200 °C for 12 h, dip-coating, Calcination: T = 450 °C for 30 min.	8–10	43
TiO_2/Ti/TiO_2-Pt *TNTs: Anatase and Pt: FCC*	E: DMSO, HCl. P: $H_2PtCl_6.6H_2O$, MetOH.	TNTs by anodic oxidation: E_{bias} = 40 V for 8 h, calcination: T = 450 °C for 3 h, Pt-NPs/TNPs by photoreduction of Pt^{4+}: T = 250 °C for 2 h.	9 (Φ = 90 nm)	49
Cu_2O/TNTs/FTO *Cu_2O: Octahedral geometry*	E: NH_4F, $Et(OH)_2$ P: $CuSO_4$	TNTs by anodic oxidation: E_{bias} = 25 V for 2 h, calcination: T = 500 °C for 1 h, Cu_2O by electrodeposition: E_{bias} = −0.4 V for 600 s at pH = 10, and calcination: T = 500 °C for 1 h.	$\Phi_{TNTs} = \Phi_{Cu\ (II)}$ = 100	52,53
α-$Bi_2Mo_3O_{12}$ /TNTs/Ti *TNTs: Anatase and α-$Bi_2Mo_3O_{12}$: tetrahedral geometry*	E: Ethylene glycol, NH_4F P: $Bi(NO_3)_3$, $(NH_4)_7Mo_7O_{24}$	TNTs by electrochemical anodization: E_{bias} 60 V for 6 h, α-$Bi_2Mo_3O_{12}$ by chemical bath deposition 2 min, and calcination: 500 °C for 3 h.	$\Phi_{outer\ TNTs}$ ca. 140 $Th_{walls\ TNTs}$ ca. 12	29
AuNP-TiO_2NA/Ti *Anatase*	E: HF, HNO_3 P: $HAuCl_4$	TNTs by electrochemical anodization: E_{bias} = 20 V for 1 h, AuNPs by electrodeposition: E_{bias} = 0 V (under sonication), calcination: 500 °C for 3 h.	$\Phi_{outer\ TNTs}$ = 60–80, $Th_{wall\ TNTs}$ = 16, L_{TNTs} = 350–380 nm, Φ_{AuNPs} = 3 ± 2.	51
3D Pt-NPs/TNTs/Ti *TNTs: Anatase*	E: Ethylene glycol, NH_4F P: H_2PtCl_6	TNTAs by electrochemical anodization: E_{bias} = 60 V for 10 min at 2.0 °C min^{-1}, calcination: 450 °C for 3 h, and Pt-NPs by electrochemical reduction: E_{bias} = −0.3 V for 3 min.	$\Phi_{outer\ TNTs}$ = 60, $Th_{wall\ TNTs}$ = 16, L_{TNTs} = 4, $\Phi_{Pt\text{-}NPs}$ = 13.	37,50
m$BiVO_4$ /FTO *Monoclinic scheelite*	E: Citric acid P: NH_3VO_4, $Bi(NO_3)_3$	Vanadium precursor: 80 °C for 15 min, hydrothermal complexation: 400 °C for 10 min, dip-coating, 10 layers, calcination: 400 °C for 4 h.	Th = 1.1–1.4 µm	78
AB@H-RTNR *Anatase and rutile*	P: Ti(i-PrO)$_4$, $[NH_4]_2TiF_6$. E: H_3BO_3	Hydrothermal: T = 170 °C for 6 h, hydrogenation: T = 350 °C for 1 h.	$\Phi_{outer\ TNTs}$ = 200, $Th_{wall\ TNTs}$ = 16, L_{TNTs} = 41.5 µm	28
CuS/TiO_2/ITO *TiO_2:Anatase and CuS: nanosheet*	P: P25 TiO_2, $CuCl_2{\cdot}2H_2O$ E: $Na_2S_2O_3{\cdot}5H_2O$	Precursor suspension was stirred in an oil bath: T = 70 °C for 4 h, natural cooling, centrifugation: 7000 rad s^{-1} for 10 min, and dried: 60 °C for 4 h	<100 nm	55
TiO_2/g-C_3N_4/ITO TiO_2: *Anatase spherical and* g-C_3N_4: *nanosheet*	P: P25 TiO_2, $C_3H_6N_6$,	ITO pretreatment and activation, Electrodeposition of Prussian blue by CV: E_{bias} = 0.4–0.8 V (vs. Hg/Hg_2Cl_2) at 100 mV s^{-1}, 25 cycles, 20 µL nanocomposites onto ITO, natural drying.	< 100 nm	54
Te-TNTs/Ti TiO_2: *Anatase spherical and* g-C_3N_4: *nanosheet*	P: NH4F, glycerol. $Te(OH)_6$, $C_2H_6O_2$.	Ti pretreatment, electrochemical anodization: E_{bias} = 25 V, 0.5 A, for 4 h. Te precursor at 150 °C for 8 h, TNT/Ti dip coating for 10 min, WE calcined at 500 °C for 90 min.	$\Phi_{inner\ TNTs}$ ca. 100 nm, $\Phi_{outer\ TNTs}$ ca. 200 nm.	48

WE working electrode, *E* electrolyte solution, *P* precursor, *HF-CVD* hot filament chemical vapor deposition, *NPs* nanoparticles, *Th* thickness, *Φ* diameter, E_{bias} bias potential, *T* temperature, *L* length, *υ* ramp, *CV* cyclic voltammetry.

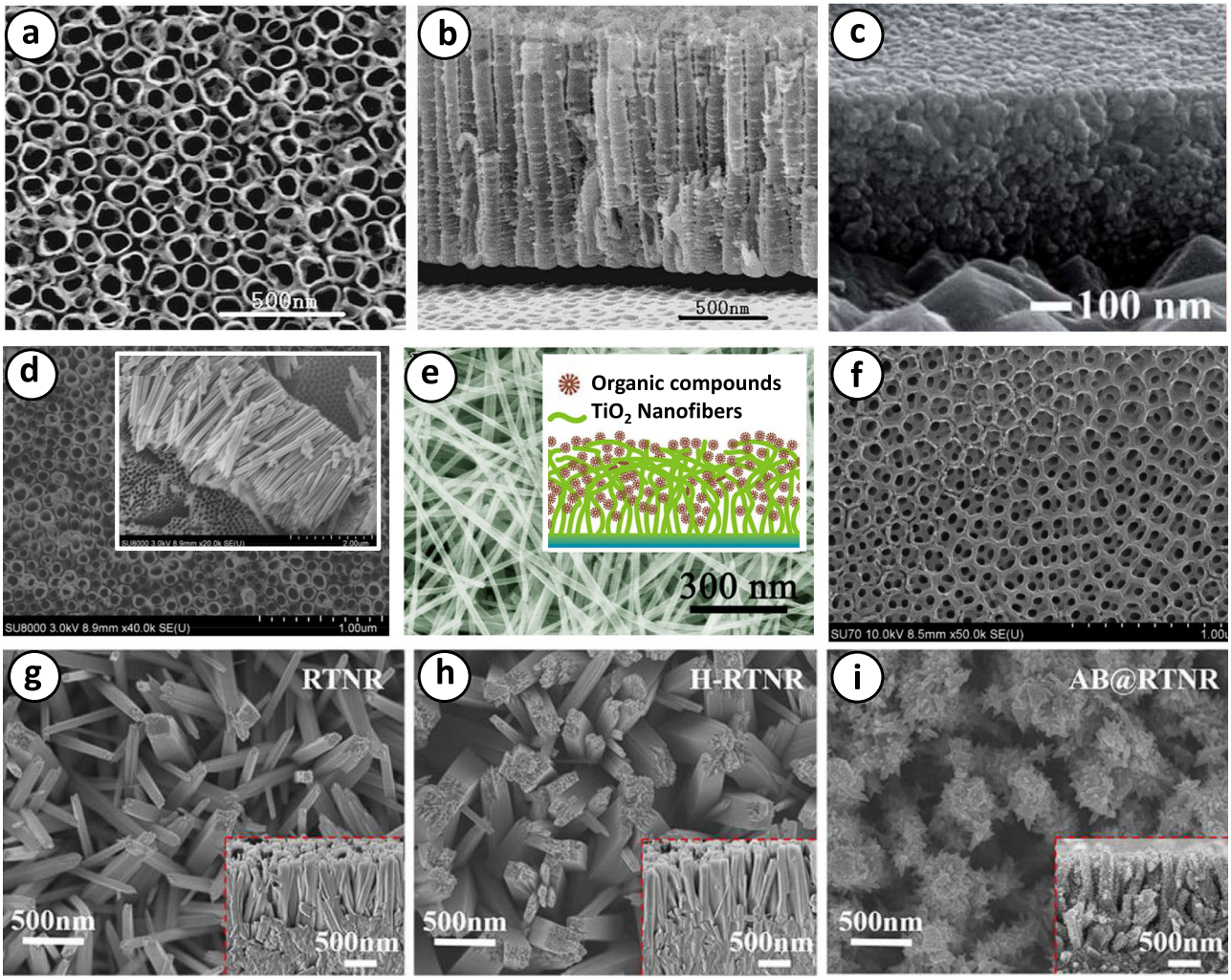

Fig. 1 | Scanning electron microscopy (SEM) images of several TiO_2 structural morphologies. a Top and (**b**) cross-sectional views of TNTs (reprinted from Zhang et al.[74]). **c** Cross-sectional view of amorphous spheres of TiO_2/boron-doped diamond (reprinted with permission from Han et al.[43] copyright 2011 Royal Society of Chemistry). **d** Top and cross-sectional (inset) views of TNTs (reprinted from Liang et al.[51]). **e** Top view of TiO_2 nanofibers with their respective interactions inserted (adapted from Mu et al.[39]). **f** Top view of TiO_2 nanopores (reprinted from Zhang et al.[68]). **g** Top view of TiO_2 nanorods (TNRs), **h** hydrogenated-TNRs, and **i** anatase-branch@hydrogenated-TiO_2-rutile nanorod (reprinted from Zu et al.[28]).

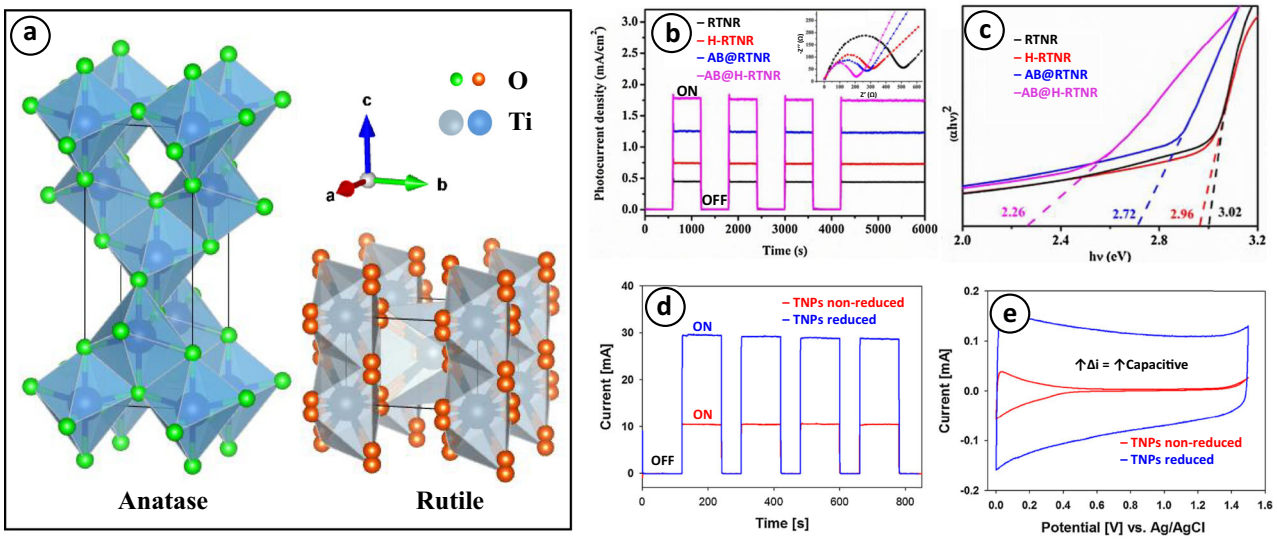

Fig. 2 | Effect on the structural modifications on the TiO_2 photoelectrodes. a Unit cells of anatase and rutile crystal structures (crystallographic parameters extracted from Materials database[76]). **b** Photocurrent density profile (Insert: Nyquist plots). **c** Tauc plots for various surface modifications of rutile-TiO_2 nanorods (RTNRs) (adapted from Zu et al.[28]). **d** Photocurrent responses and **e** cyclic voltammetry of reduced effect for TiO_2 nanopores (TNPs) (adapted from Zhang et al.[68]).

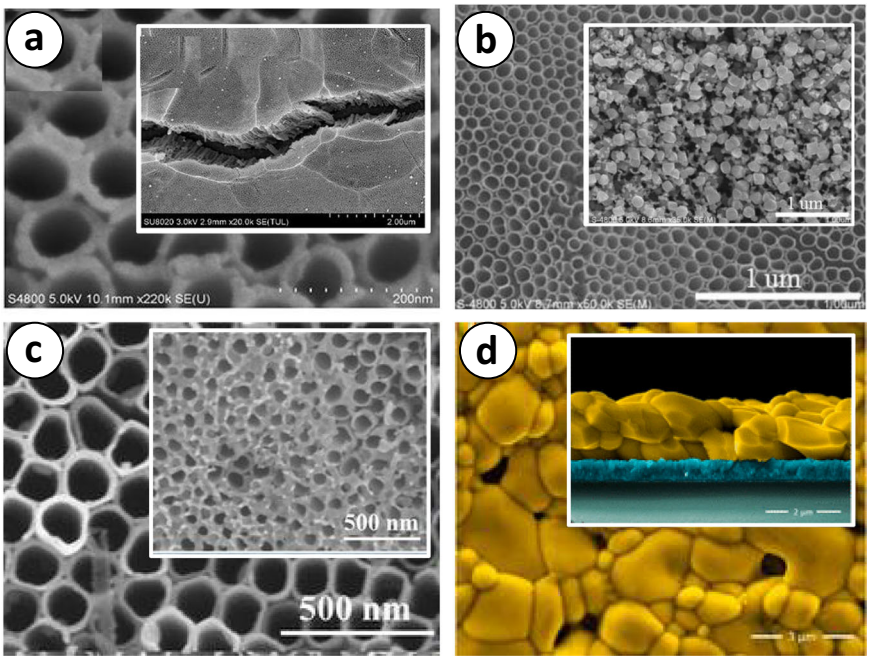

Fig. 3 | SEM images of combined and hetero-structured nanomaterials. Top views of TiO_2 nanotubes (TNTs) before modification with inserts of: **a** AuNPs/TNTs/Ti (adapted from Si et al.[50]), **b** Cu_2O/TNTs/Ti (adapted from C. Wang et al.[52]), **c** α-$Bi_2Mo_3O_{12}$/TNTs/Ti (adapted from Pang et al.[29]) and **d** m$BiVO_4$/FTO (cross-sectional inset; adapted from Alves et al.[78]).

resulting in the Cu_2O/TNT/Ti composite. The octahedral Cu_2O coating on the TNTs improves the PEC properties, as indicated in Fig. 4a and b. This modification increases photocurrent density by 60% and stabilizes the electrode over time at a constant value of approximately 0.25 mA under light-ON conditions (Fig. 4a) while decreasing the charge transfer resistance (R_{CT}) of delta by ~700 Ω (see diagram in Fig. 4b). Accordingly, the Cu_2O/TNT/Ti photoanode has more efficient electron-hole pair separation compared to TNTs alone, allowing simultaneous processes (Eqs. 1 – 6) to occur under visible light (Fig. 4b)[52].

Moreover, the applicability of PEC-COD sensors using nanomaterials extends to bismuth-based ternary oxides such as molybdates[29] and vanadates[78], which show good PC behavior under visible light, high stability, and non-toxicity. Bismuth molybdates, with the formula $Bi_2O_3.nMoO$, differ in terms of the composition of their α, β, or γ phases (if "*n*" is 3, 2, or 1, respectively), depending on the proportions of Bi and Mo[79]. For instance, high Mo concentrations at acidic pH produce scheelite nanostructures of the α-$Bi_2Mo_3O_{12}$ phase, characterized by molybdates with tetrahedral geometry (see Fig. 4d). In contrast, high Bi concentrations and alkaline pH yield fluorite and Aurivillius structures of the β- and γ-$Bi_2Mo_3O_{12}$ phases[80,81]. During synthesis, particle size, structure, and morphological homogeneity can be strategically controlled using surfactants like polyvinylpyrrolidone and cetyltrimethylammonium bromide, which enhance the PC activity of alpha bismuth molybdate. It is also possible to create one-dimensional structures like nanorods, nanotubes, or nanobelts and two-dimensional structures like nanosheets or nanoplates via hydrothermal, solvothermal, or glycothermal methods at low temperatures. For these nanomaterials, higher calcination temperatures between 450 and 550 °C result in lower E_{BG} [79,80].

For instance, the PEC-COD sensor developed by Pang et al.[29] improved the properties of the TNTs/Ti via α-$Bi_2Mo_3O_{12}$ immersion deposition, resulting in the working electrode α-$Bi_2Mo_3O_{12}$/TNTs/Ti (see Table 1 for more specific parameters). This modification improved the photoinduced charge separation, reducing the R_{CT} from over 1000 Ω for TNTs/Ti under light to ~100 Ω for α-$Bi_2Mo_3O_{12}$/TNTs/Ti under light (Fig. 4c). This improvement is attributed to the decrease in E_{BG} from 3.43 eV to 3.23 eV from the modification, with the E_{VB} becoming less positive, shifting from 3.09 eV to 2.41 eV[29]. This shift is due to the E_{VB} being formed by the 4 d and 6p orbitals of Mo and Bi, respectively, and the CB by the O 2p orbital[29,80].

In another study[78], the n-type semiconductor $BiVO_4$, with 2.4 eV of E_{BG} in its monoclinic scheelite nanostructure and a E_{VB} of 2.86 eV, was applied to fluorine-doped tin oxide (FTO). $BiVO_4$ is notable for its broad-spectrum PEC oxidative ability under visible light, exhibiting high charge transfer separation efficiencies, which facilitates its use as a working electrode for photochemiresistors[70,78]. The high photoinduced charge carrier separation efficiency of m$BiVO_4$ is also due to the spatial arrangement on the nanomaterials' crystal surfaces. Additionally, Ding et al.[82] theoretically showed that the water adsorption and photoelectrooxidation mechanisms for m$BiVO_4$ are promoted on the crystalline surfaces {100} and {110}.

The m$BiVO_4$ structure consists of dodecahedral BiO_8 units surrounded by tetrahedral VO_4 units, connected by a shared vertex oxygen (see Fig. 4e). The band structure and DOS are illustrated in Fig. 4f, which shows the theoretical energetic edge positions of m$BiVO_4$ boundary bands. These positions correlate with the corresponding chemical bonds, where the oxygen 2p orbital is the primary charge donor in the VB, overlapping the total DOS. Additionally, the distribution of orbitals with the electronic band structures reveals V-O and Bi-O bonding mechanisms located in the 6 s, 2p, and 3 d orbitals for Bi, O, and V, respectively[82].

$$\text{Semiconductor} + h\nu\left(\geq E_{BG}\right) \rightarrow \text{Semiconductor}\left(h^+_{VB} + e^-_{CB}\right) \quad (1)$$

$$TiO_2 + h\nu(\geq 3.2eV) \rightarrow TiO_2\left(h^+_{VB} + e^-_{CB}\right) \quad (2)$$

$$\text{Semiconductor}\left(e^-_{CB}\right) + TiO_2 \rightarrow TiO_2\left(e^-_{CB}\right)(\textit{depends on CTMs}) \quad (3)$$

$$h^+_{VB}\left(\text{SC and}TiO_2\right) + H_2O \rightarrow HO^{\bullet} + H^+ + e^- \quad (4)$$

$$h^+_{VB}(\text{SC and}TiO_2) + \text{OM} \rightarrow \text{byproducts} \rightarrow CO_2 + \ldots + H_2O\,(\textit{direct oxidation}) \quad (5)$$

$$HO^{\bullet} + \text{OM} \rightarrow \text{byproducts} \rightarrow CO_2 + \ldots + H_2O\,(\textit{indirect oxidation}) \quad (6)$$

In the context of COD detection using nanomaterials, the choice of conductive substrates also plays an important role in sensor stability and reproducibility. BDDs have demonstrated numerous advantages over other conductive materials such as iridium tin oxide (ITO), FTO, and metals such as Ti. These advantages include a wide electrochemical working potential window, high mechanical strength, corrosion resistance, and stability. The

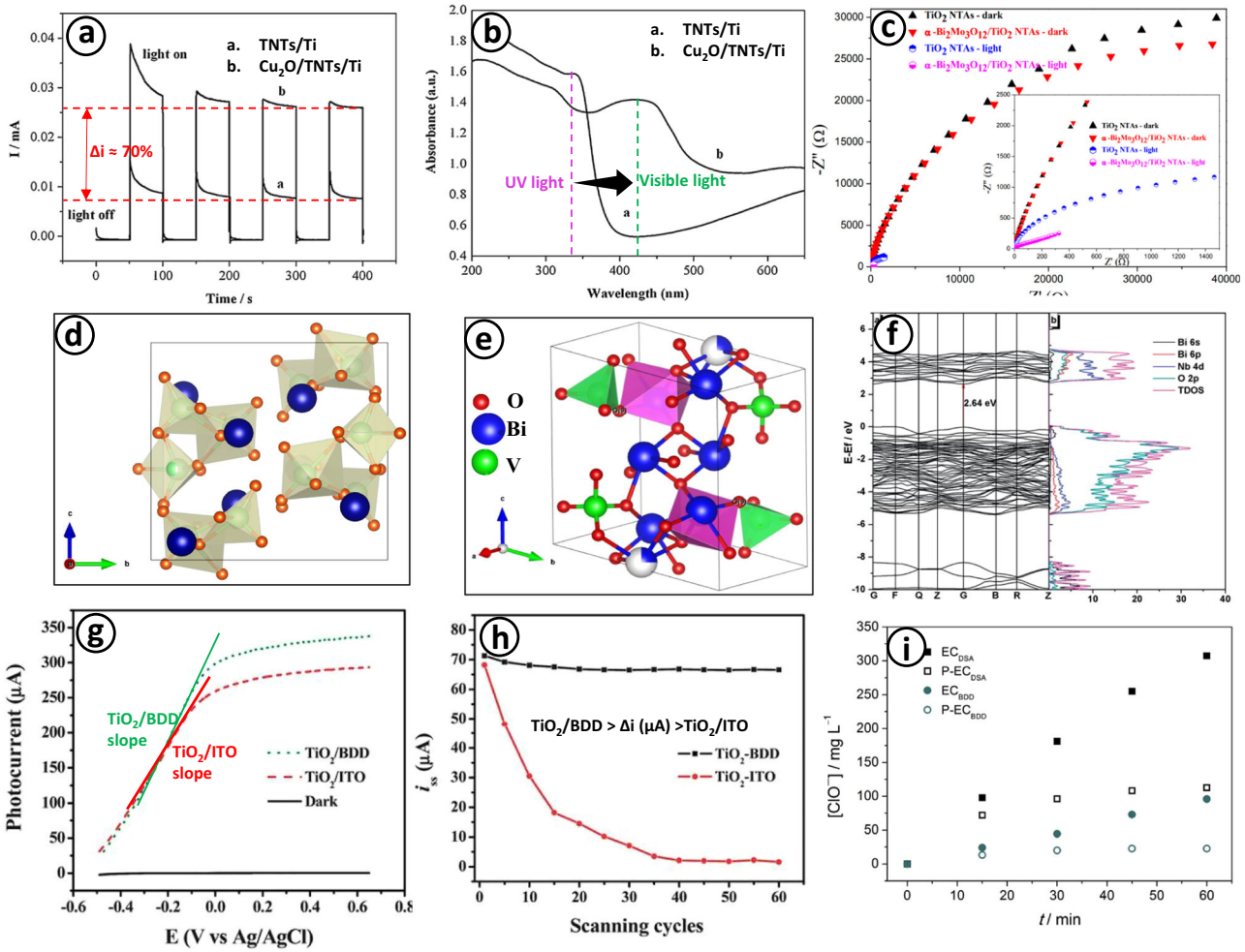

Fig. 4 | Characterization and properties of WEs with photocatalytic activity. **a** Photocurrent profiles and **b** ultraviolet–visible absorption spectrum of TNTs/Ti and loaded-Cu_2O TNTs/Ti with a Nyquist plot (inset; adapted from Wang et al.[52]). **c** Nyquist plot (Insert: zoomed plot, reprinted from Pang et al.[29]) and **d** geometric disposition of α-$Bi_2Mo_3O_{12}$/TNTs/Ti (crystallographic parameters extracted from Pang et al.[29]). **e** Crystal structure (crystallographic parameters extracted from Crystallography Open database), **f** band structure, and density of states for $BiVO_4$ (Ding et al.[82]). **g** Linear sweep voltammetry profile and **h** acid stability curves from cyclic voltammetry for TiO_2/BDD and TiO_2/ITO (adapted from Han et al.[43]). **i** Hypochlorite anion concentration based on advanced oxidation process treatments using BDD and dimensionally stable anodes (DSA) (reprinted from Sánchez-Montes et al.[83]).

performance of BDDs depends on factors including the amount of impurities in the doping process, particularly the amount of boron and the presence of Csp^2 in the crystalline structure. These characteristics can be examined using Raman spectroscopy, where the characteristic absorption intensity of BDDs is approximately 1333 cm^{-1}[44,85–89].

For instance, Han et al.[43] demonstrated the superior charge separation efficiency of BDD over ITO through a comparative photocurrent and potential curve analysis between TiO_2/BDD and TiO_2/ITO. They obtained the I_{ph} - E curve (Fig. 4g), which showed a more positive slope in the rising zone for BDD, indicating BDD requires less energy than ITO to separate photoinduced electrons. This results in a more efficient extraction of photogenerated electrons from TiO_2, as well as high stability of the TiO_2/BDD combination, as shown in Fig. 4h[43,84]. Furthermore, Sánchez-Montes et al.[83] compared the production of active chloride species (ACSs) under UV-C light between BDD and dimensionally stable anodes (DSAs). Figure 4i shows that BDD produces fewer ACSs compared to DSAs because of BDD's larger overpotential window[83,88,89].

PC-COD and PEC-COD sensors

The applicability of PC-COD and PEC-COD sensors is contingent upon their stability and reproducibility. To be considered valid and comparable to conventional methods such as spectrophotometry, these sensors must have relative standard deviation percentages (%RSD) of less than 5%. Achieving this necessitates the consideration of the PC properties of nanomaterials, the operational variables in sensors, and the production of active species.

For PC-COD-sensors, spontaneous ($\triangle G<0$) PC oxidation processes occur only if the photogenerated E_{VB} or its hole potential (h^+_{VB}) is more positive than the standard oxidation potential of the species of interest. In the case of water, a h^+_{VB} more energetic than +2.40 eV is required to produce hydroxyl radicals, which are considered effective and sustainable oxidants given their highly non-selective and exhaustive reactivity.

Regarding PEC activity in PEC-COD sensors, the PC condition is not essential for achieving the desired outcome. Through electrochemical charge polarization, the band alignments within the depletion region can be sufficiently bent to facilitate the redox process; in other words, while the position of the catalyst's potential in the band energy diagram does not limit the method, it serves as a valid criterion for minimizing energy consumption, particularly when using solar energy as the primary source.

Further, fine-tuning the operating variables enables accurate and reliable results across a broad sensing range. For instance, variations in system temperature from light sources or electron-hole recombination can lead to fluctuations in current densities due to semiconductor overload, potentially compromising method reproducibility. Therefore, maintaining stable room temperature conditions is advisable.

The presence of ACSs such as HClO, $Cl^{\cdot}$, and $ClO^{\cdot}$ [74,88] and active sulfate species (ASSs) such as SO_4^{2-}, $SO_4^{\cdot-}$, $yS_2O_8^{2-}$ [12,86,92] affect sensors'

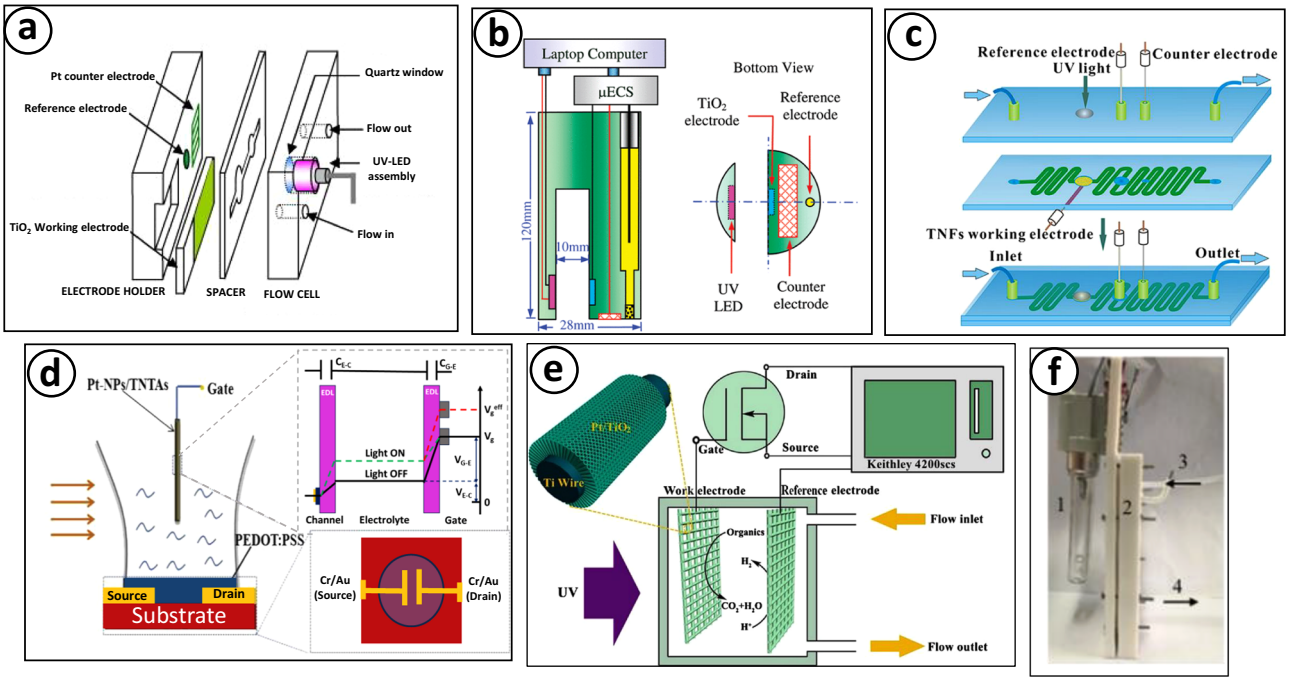

Fig. 5 | Schematic representation of PEC-COD sensor platform. a UV-LED portable thin-layer sensor (reprinted from Zhang et al.[94]). **b** Portable setup (reprinted from Zhang, Li, and Zhao[72]). **c** Microfluidic device (reprinted from Mu et al.[39]). **d** Electrochemical transistor (adapted from Liao et al.[77]. **e** Extended-gate field-effect transistor sensor (reprinted from Si et al.[37]). **f** prototype of a real cell for real-time determination by PEC-COD-sensor, which includes: 1. UV lamp, 2. electrode compartment, 3. flow inlet, 4. flow outlet (reprinted from Si et al.[50]).

detection performance. ACSs can be produced through C-type ultraviolet radiation induced homolysis of HClO and subsequent oxidation via $HO^{\cdot}$ and $Cl^{\cdot}$ (Eqs. 7 and 8)[74]. On the other hand, ASSs are produced via direct and indirect electrooxidation of sulfuric acid or sodium sulfate (Eqs. 9–12)[86,92]. In fact, Zhang et al.[74] demonstrated that when Cl^{-} and NH_4^{+} ion concentrations exceed 500 mg L^{-1}, the results are not reproducible, whereas concentrations below this level allow for feasible and reproducible quantification.

$$HClO + HO^{\cdot} \rightarrow H_2O + ClO^{\cdot} \quad (ACSs) \tag{7}$$

$$Cl^{\cdot} + ClO^{\cdot} + H_2O \rightarrow 2HCl \quad (ACSs) \tag{8}$$

$$2SO_4^{2-} \rightarrow S_2O_8^{2-} + 2e^{-} \quad (Direct\ oxidation\ AASs) \tag{9}$$

$$HSO_4^{-} \rightarrow S_2O_8^{2-} + 2e^{-} \quad (Direct\ oxidation\ AASs) \tag{10}$$

$$HSO_4^{-} + HO^{\cdot} \rightarrow SO_4^{\cdot -} \ (Indirect\ oxidation\ AASs) \tag{11}$$

$$H_2SO_4 + HO^{\cdot} \rightarrow SO_4^{\cdot -} \ (Indirect\ oxidation\ AASs) \tag{12}$$

It is important to note that sensor limits and ranges of detection are influenced by the extent of water contamination[16]. Additionally, the reproducibility and repeatability of sensor measurements are also affected by the presence or absence of macromolecules such as suspended solids; thus, it is recommended that wastewater be filtered prior to COD measurements[27].

PC-COD sensors

Analytical principle

PC-COD sensors operate on the principle of photocatalysis, which has been extensively studied[16,19–21]. Research has demonstrated that the mineralization of organic pollutants and their quantitative determination via photocatalysis relies on the coupling of the anatase TiO_2 semiconductor ($E_{BG(TiO_2)} = 3.2eV$) with oxidizing agents such as $K_2Cr_2O_7$[19], $Ce(SO_4)_2$[21], and $KMnO_4$[16]. These agents act as electron scavengers, capturing photoinduced electrons from the CB (e^{-}_{CB}) and simultaneously reducing to Cr^{3+}, Ce^{3+}, and Mn^{2+}, respectively (Eqs. 13–15)[69]. This synergistic interaction produces an analytical signal that correlates with the absorbance and COD, thereby minimizing electron-hole recombination kinetics[19,21,69].

$$Cr_2O_{7(aq)}^{2-} + 14H_{(aq)}^{+} + 6e^{-} \rightarrow 2Cr_{(aq)}^{3+} + 7H_2O_{(l)} \quad (E^0_{Cr^{6+}/Cr^{3+}} = 1.33V) \tag{13}$$

$$Ce_{(aq)}^{4+} + e^{-} \rightarrow Ce_{(aq)}^{3+} \quad (E^0_{Ce^{4+}/Ce^{3+}} = 1.61\ V) \tag{14}$$

$$MnO_{4(aq)}^{2-} + 8H_{(aq)}^{+} + 5e^{-} \rightarrow Mn_{(aq)}^{2+} + 4H_2O_{(l)} \quad (E^0_{Mn^{7+}/Mn^{2+}} = 1.51V) \tag{15}$$

Cesium sulfate acts as an effective electron scavenger with a stronger oxidizing capacity compared to permanganate and dichromate, following the trend $E^0_{Ce^{4+}/Ce^{3+}} > E^0_{Mn^{7+}/Mn^{2+}} > E^0_{Cr^{6+}/Cr^{3+}}$, (cf. Eqs. 13–15). When coupled with TiO_2, $Ce(SO_4)_2$ demonstrates superior detection performance in PC-COD sensors compared to TiO_2-$KMnO_4$ or TiO_2-$K_2Cr_2O_7$ couplings. Specifically, TiO_2-$Ce(SO_4)_2$ coupling is up to five times more effective in oxidizing OM during the initial minutes compared to individual TiO_2 or $Ce(SO_4)_2$ under the same conditions[21]. This coupling improves testing times and expands the electron scavenger's applicability[21]. Additionally, Zhu et al.[16] proposed the surface fluorination of TiO_2 ($\equiv Ti-F$), which improves oxidation rates by promoting strong interactions between hydroxyls and fluorides, thereby increasing hydroxyl radical production (Eqs. 16 and 17).

$$\equiv Ti - OH + F^{-} \rightarrow \equiv Ti - F + HO^{-} \tag{16}$$

$$\equiv Ti - F + H_2O + h_{VB}^{+} \rightarrow \equiv Ti - F + HO + H^{+} \tag{17}$$

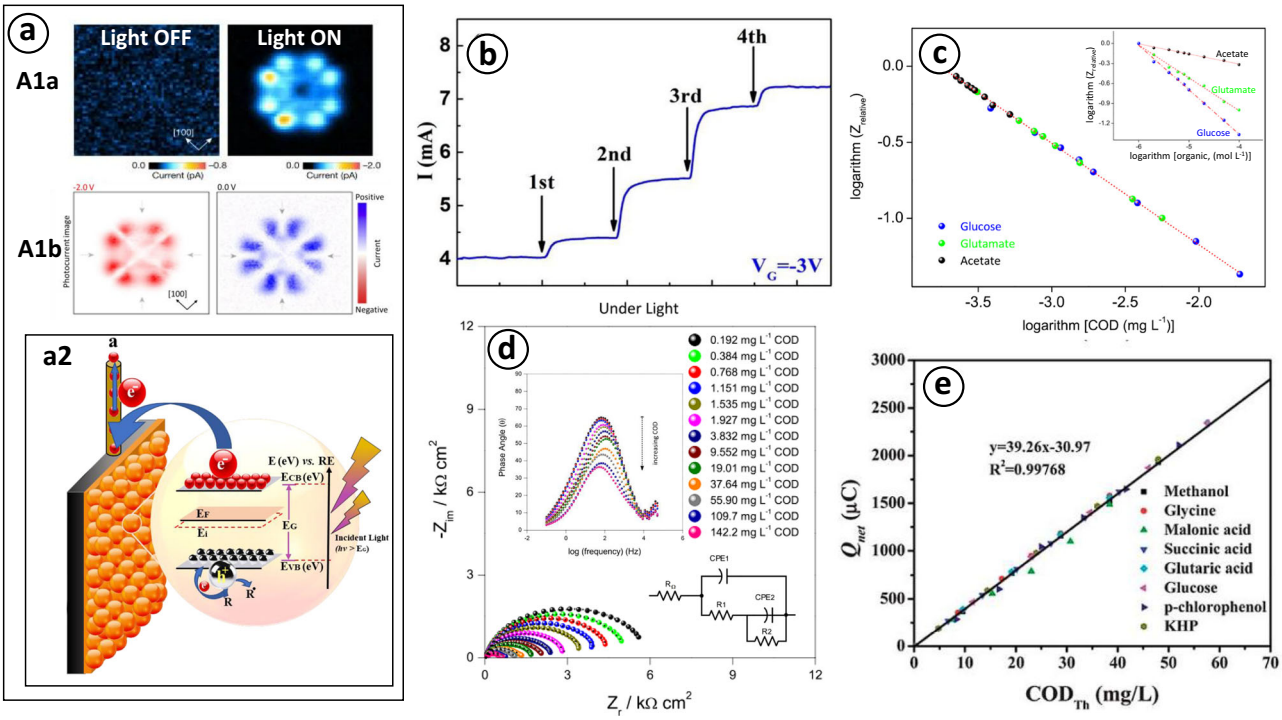

Fig. 6 | Schematic representation of the PEC principle and PEC-COD analytical curves. a1 Images of photoinduced molecular excitation effect (reproduced from Imai-Imada et al.[65] and **a2** Schematic diagram of photocurrent generation. **b** Photocurrent response using the amperometry method with COD addition (reprinted from Si et al.[37]). **c** calibration curve from photochemiresistor sensor (Insert: analytical curves with different organic analytes, adapted from Alves et al.[78]). **d** Nyquist plot with inset of Bode diagram with different COD aliquots (adapted from Alves et al.[78]). **e** validation curve between conventional and PEC-COD sensor (adapted from Han et al.[43]).

Operational variables that affect PC-COD sensors

The selection of an appropriate pH range is crucial and depends on the point of zero charge (PZC) of photocatalysts and the standard oxidation-reduction potential (E^0_{REDOX}) of the oxidizing agent (electron scavenger). When PZC < pH, the surface of the material becomes electropositively charged, promoting PC oxidation. Research has demonstrated that a pH ≤ 2 increases PC oxidation capacity[16,19–21]. For instance, the absorbance and pH correlation for $K_2Cr_2O_7$ shows an increasing trend in the range of 0.5 ≤ pH ≤ 1.5, with a notable concavity change observed beyond this range, attributed to the distribution of $Cr_2O_7^{2-}$ and $HCrO_4^-$ [19]. In another study[20], a pH of 5.6 was selected for the $(MnO_4)^{2-}$ anion, aligning with the PZC values of ZnO and TiO_2 (6.0 and 5.8, respectively); the study found that at a pH < 5, ZnO does not act as an amphoteric oxide, promoting homogeneous catalysis reactions dominated by $KMnO_4$. Further, Zhu et al.[19] examined the PZC of TiO_2 and the degree of fluorination, determining that at pH < 3, fluoride anion concentration decreases owing to the weak acidity of fluoric acid, consequently reducing the fluorination degree of titanium (≡ Ti − F). Additionally, pH values above 3 decrease the concentration of permanganate[16,20].

Control over the photocatalyst and electron scavenger dose optimizes oxidation processes and PC quantification; an excessive quantity of nanoparticles in suspension may introduce interferences during ultraviolet–visible spectrum generation, attributed to the Tyndall effect. For example, Ai et al.[19] demonstrated a directly proportional correlation between absorbance and TiO_2 dose up to an inflection point of 0.04 mg L^{-1}, after which the curve became pseudo-constant or asymptotic. This critical concentration of 0.04 mg L^{-1} has been identified as optimal, and higher concentrations have been shown to decrease detection effectiveness due to an excess of suspended nanoparticles[16,19–21].

The dosage of permanganate also influences the limits and ranges of detection according to the degree of water pollution[16,20]. For instance, Zhu et al.[16] observed that increasing permanganate concentrations from 1 to 10 mmol L^{-1} altered detection limits from 0.02 to 20 mg L^{-1}, respectively, achieving average efficiencies of 99% in both cases. Similarly, the amount of $KMnO_4$ reduced also depends on UV exposure time, which diminishes after the initial 10 min[20]. Regarding TiO_2 fluorination, Zhu et al.[16] achieved maximum absorption when fluoride concentration reached 5 mmol L^{-1}, with negligible chloride interference at concentrations below 1000 mg L^{-1}.

PEC-COD sensors

The pioneers in PEC-COD sensors are the research groups led by Zhang and Zhao in 2004[44,91,93]. Currently, PEC oxidation processes are well-established in this field given their high efficiencies and substantial impact, combining electrochemical assistance with photocatalysis. Recent advancements in PEC-COD sensors are depicted in Fig. 5a–f, showcasing various distinguishing characteristics. These sensors aim to convert electrochemical variables into OM quantities, providing real-time COD values that are applicable across diverse practical scenarios.

Analytical principle

COD quantification through PEC processes is based on the combustion of OM, where the 1:1 stoichiometric relationship between OM ($C_yH_mO_jN_kX_q$) and consumed oxygen $(4y - 2j + m - 3k - q)$ transfers electrons, as described in (Eq. 18). As illustrated in Fig. 6a2, these photoinduced electrons can be extracted and detected using electrochemical methods such as voltammetry, impedance, or chronoamperometry; the photocurrent signal is mathematically correlated to the amount of mineralized OM by Faraday's law, expressed in terms of oxygen (Eqs.

19 and 20)[44,91].

$$C_yH_mO_jN_kX_q + (2y-j)H_2O \ldots \rightarrow yCO_2 + qX^- + kNH_3 + (4y-2j+m-3k)H^+ \ldots + (4y-2j+m-3k-q)e^- \quad (18)$$

$$Q_{Photocurrent} = Q_{total} - Q_{Blank} = \int_0^t Q_{net}\,dt = nFVC; \left[n_{C_yH_mO_jN_kX_q} = \ldots(4y-2j+m-3k-q)e^-\right] \quad (19)$$

$$COD\left(mg\,L^{-1}\,O_2\right) = \frac{Q_{Photocurrent}}{4FV} * 32000;\ \left(COD \propto Q_{Photocurrent}\right) \quad (20)$$

Based on these analyses, Alves et al.[78] developed a photochemiresistor sensor using impedance spectroscopy. This technique allowed them to correlate changes in the capacitive and resistive behavior of the material, specifically the resistance to organic charge transport at the mBiVO$_4$/FTO solution interface, under both light and dark conditions. Nyquist and Bode plots revealed a decrease in resistance and phase angle, respectively, with increasing COD concentrations, which was described using electrical equivalent circuit (EEC) (Fig. 6d). They further established a mathematical correlation (Eq. 21) between the relative impedance $Z_{Relative}$ and the logarithm of COD concentrations (Fig. 6b, c). This correlation normalized the impedance response with light (Z_m) and without OM (Z_o), at a frequency of 0.1 Hz, covering organic doses between 4 and 20 mg L^{-1}. This approach aimed to improve sensitivity and response time during the validation stage (Table 2).

$$\log\left(Z_{Relative}\right) = m\log(COD) + b;\ \left(Z_{Relative} = \frac{Z_m}{Z_o}\right) \quad (21)$$

Similarly, other studies[37,50,77] have developed online PEC detectors based on the extended-gate field-effect transistor sensor (see Fig. 5d–f). These studies correlated the channel potential of the transient $(V_{G-chanel})$, gate electrode (V_G), and molal organic concentration, as described in (Eq. 22), to determine the charge quantity Q in the transient channel. Here, C is the material capacitance, k is Boltzmann's constant, T is temperature, n is the number of electrons transferred, and A and α are compilations of constants[37,50]. Zhang et al.[94] further improved the feasibility of PEC-COD sensors by integrating them with computer software, allowing analysts to control all process variables (Fig. 5b). This setup enabled the generation of amperograms, as shown in Fig. 6b, demonstrating the linear behavior of the I$_{ph}$-COD (Fig. 6c and e).

$$I_{neta} = \frac{C\left[V_G + 2.30\left(\frac{kT}{nq}\right)\log C_m - A'\right]}{\triangle t} = \alpha\log(C_m) + A;\ ([COD] = 8000nC_m) \quad (22)$$

Influence of operational variables on PEC-COD sensors

Bias potential is inversely proportional to the electron-hole recombination rate. According to the theoretical principles, necessary energy supply enables the detection of photogenerated electrons. Applying a suitably positive charge bias potential thus theoretically allows the quantification of $(4y-2j+m-3k-q)e^-$ in the oxidation of one mole of $C_yH_mO_jN_kX_q$, as described in (Eq. 18)[72]. A sufficiently positive potential is defined as a value or range of applied potentials in which a set of processes occur (Fig. 6d). In the case of PEC-COD sensors, it is crucial to consider the potential characteristic of hydroxyl radical evolution, which varies depending to the intrinsic and extrinsic properties of the material used. For instance, the applied oxidation potential for water on a BDD substrate is higher than that on Pt. The trend of the *I-E* curve is directly proportional[51]. However, based on the behavior of the points in Fig. 7a, the following should be considered:

i. When working in an increasing potential range within −0.4 < E (V *vs.* Ag/AgCl) < 0.2, collecting photogenerated electrons in the oxidation process is the determining step.
ii. When the *I-E* curve behavior is approximately constant between 0.4 < E (V *vs.* Ag/AgCl) < 0.8, interfacial oxidation is the determining step. This step controls the rate of the PEC oxidation process, suggesting that all photogenerated electrons are extracted, detected, and quantified.
iii. High potentials can generate surface interferences because of possible photocorrosion or gas evolution[46,91].

The acid resistance of PEC-COD sensors is key for monitoring wastewater with acidic matrices. Changes in acidity at the working electrode can modify the flat band potential and the band-edge, impacting the reproducibility of the sensor. At specific acidic pHs, substrates such as ITO and Ti exhibit low acid resistance owing to their chemical nature, limiting their application and reliability. In contrast, BDD has excellent acid resistance, as shown in the comparative curves in Fig. 7b, c[43].

According to the Fig. 7c, when pH < 2, conductive substrates such as ITO and FTO lose conductivity; at 2 < pH < 4, the current and pH correlation increases, indicating that the electrode is not yet stable, and results are not reproducible in this pH range. Indeed, the organic charge obtained in this range is lower than theoretically calculated. However, when pH > 10, the Q_{blank} increases and the Q_{net} decreases because of the photoelectrooxidation of water, which is facilitated at alkaline pH[84]. Thus, when 4 < pH < 10, the charges are approximately constant and equal to the theoretical value[44,72].

During the calibration stage, the organic load concentration influences the sensitivity of PEC-COD sensors. Zhang et al.[45] used a flow system for quantification and calibration with their COD sensor, finding that the correlation between organic load and concentration at different flow rates was linear during the degradation of the organic analyte, such as glucose. At lower flow rates, the slope of the correlation was higher, indicating the method becomes less sensitive as the mass transfer rates to the interface increase. Conversely, higher injection volumes of the analyte improved the detection limit and sensitivity, although this reduced the detection range (Fig. 7c and d)[45].

The photocurrent is the result of charge transfer due to photoinduced electron movement over time[40]. This phenomenon was examined by Imai-Imada et al.[65], who used a scanning tunneling microscope to observe atomic-level charge distribution and photocurrent channels between orbital lobes and nodes in light and dark conditions (Fig. 6a1a, inset graph). The dependence of charge flow and the charge's spatial distribution on the polarization potential is also observed (Fig. 6a1b, inset graph). Under darkness, the current density tends to zero or remains negligible compared to the photocurrent under UV light (Fig. 7e). This increase in current, known as the photocurrent or net charge (Q_{net}), is mathematically represented as the area under the total current curve (Q_{total}) minus the blank (Q_{blank}) (Eqs. 19–20). Here, Q_{Blank} is the result of water oxidation, while Q_{total} includes the charge contribution from both PEC-COD light and OM oxidation. Therefore, Q_{total} has a direct relationship with OM concentration and light intensity, influenced by the altered kinetics of negative carrier transfer during the process of organic photoelectrooxidation[91].

As illustrated in Fig. 7d, Zhang et al.[44] determined that an increase in light intensity proportionally increases both Q_{total} and Q_{blank} while simultaneously increasing the linear detection range and maintaining a constant Q_{net} interval. This indicates that light intensity does not interfere with OM analyte detection and helps reduce assay times. However, if the linear range increases with higher light intensities, reproducibility can decrease because of possible interference from gas photogeneration or photocorrosion, which can affect electrode stability. Consequently, light intensity is a key experimental variable (see Table 2); the optimal intensity is determined by the inflection point of the analyte concentration and photocurrent curve at different light intensities. For example, Zhang, Li, Zhao[94] recommended using an intensity of 9 mW cm^{-2} for TiO$_2$, as they found lower light intensities are preferable to maintain a constant linear range between Q_{net} and Q_{blank}[44,91].

Table 2 | Quantification results with corresponding operational conditions for PEC-COD sensors

Cell setup	Operational conditions	DL (mg L^{-1})	RD	Linear regression	Ref
WE: TiO_2/ITO, SE: $NaNO_3$, CE: Pt. RE: Ag/AgCl, and Xe lamp	TiO_2 monolayer: Th = 0.18 mm, A = 0.75 cm^2, anodic compartment: V = 13.5 µL at 23 °C, E_{bias} = +0.3 V (*vs.* Ag/AgCl), I_{light} = 6.6 mW cm^{-2} (P = 150 W), and t_{assay} = 1–5 min	0.2 *(1.2% RSD)*	≤200	PEC-COD = 0.9957 ThCOD – 0.2333 (R^2 = *0.990, calibration)*. PEC-COD = 1.0040 COD—0.0384 (R^2 = *0.987, n = 15) (std)*	44,90
	TiO_2 monolayer: Th = 0.10 mm, A = 0.785 cm^2, anodic compartment: V = 7.85 µL at 23 °C, E_{bias} = +0.2 V (*vs.* Ag/AgCl)		0.2–360	PEC-COD = 1.024 COD *(std, R^2 = 0.992, n = 28)*	
WE: TiO_2/ITO, CE: Pt, SE = $NaClO_4$ flux	E_{Bias} = +0.3 V (*vs.* Ag/AgCl), J_{rate} = 0.3 mL min^{-1}, V = 13 µL at 23 °C.	1 *(0.8% RSD)*	≤100	PEC-COD = 1.0145 ThCOD + 0.3192 (R^2 = *0.9895)*	45
WE = TiO_2/ITO, SE = $NaNO_3$	TiO_2 monolayer: A = 0.2 cm^2, anodic compartment: V = 2.0 µL at 23 °C, $d_{(RE-WE)}$ = 3 mm, $d_{(RE-WE)}$ = 4 mm, E_{Bias} = +0,3 V (*vs.* Ag/AgCl), $I_{UV-light}$ = 9.0 mW cm^{-2} (2.0 W), and pH 4–10	0.2 *(1.55% RSD)*	≤300	Q_{net} = 0.0242 COD + 0.0125 (R^2 = *0.9985)* PEC-COD = 0.989 ThCOD (R^2 = *0.997, n = 24)*	72
WE = TiO_2/Ti, SE = Na_2SO_4, UV-type lamp	E_{bias} = +0.5 V (*vs.* SCE), $t_{current\ stead\ state}$ = 30 s, pH 8, V = 50 µL	16 *(6.8% RSD)*	50–2000	i_{net} = 0.0085 COD—0.0596 (R^2 = *0.9990)* CrCOD = 1.0095 COD PEC-COD, (R^2 = *0.9895, n = 25)*	96
WE: Ti/TiO_2, CE: Pt_{disk}, SE = Na_2SO_4	$\Phi_{Under\ UV\ illumination}$ = 1.5 mm, E_{bias} = +0.6 V (*vs.* SCE), pH 6, J_{Rate} = 1.0 mL min^{-1}	5	50–1000	PEC-COD = 0,9345 CrCOD + 12.7726, *(n = 20,* R^2 = *0.9961)*	46
WE: TiO_2, SE = $NaNO_3$, CE = Pt	T_{assay} = 23 °C, I_{Ligth} = 20 mW cm^{-2}, E_{bias} = +0.3 V (*vs.* Ag/AgCl, pH 3–10	0.2 *(1.9% RSD)*	≤ 120	i_{net} (mA) = 0.000698 ThCOD + 0.00263 (R^2 = *0.9865);* PEC-COD = 1.02 COD (R^2 = *0.993, n = 20)*	94
WE = TiO_2/FTO, CE = Pt_{wire}	I_{Light} = 1.2 mW cm^{-2} (4 W), E_{Bias} = 0.4 V (*vs.* Ag/AgCl)	1 *(3.56% RSD)*	≤ 130	i_{net} (mA) = 0.028 ThCOD + 0.024 (R^2 = *0.9951, n = 30)*	40
CE = Pt_{foil}, SE = $NaNO_3$ Visible light illumination	I_{Light} = 1.2 mW cm^{-2} (230 W), E_{Bias}, E_{Bias} = 0.10 V (*vs.* Ag/AgCl), t_{Steady} = 40 s	3.0	≤ 288	Q_{net} = 0.0886 PEC-COD + 0.0284 (R^2 = *0.996)* PEC-COD = 1.0004 COD + 1.129 (R^2 = *0.985)*	42
WE: TiO_2, SE = $NaNO_3$	$t_{Determination}$ = 5 min, $E_{bias\text{-}choronoamperometric}$ = 0.4 (*vs.* Ag/AgCl), $P_{UV-illumination}$ = 6.6 mW cm^{-2}, Φ_{WE} = 6 mm, $C_{COD\ solution}$ = 50 mg L^{-1}	0.12 *(1.5% RSD)*	≤ 300	PEC-COD = 1.0027 COD—0.0365 (R^2 = *0.9977, n = 20)*	43
SE = $NaSO_4$	150 W Xe-lamp/30 min, pH = 6.3, $I_{UV-light}$ = 2.0 mW cm^{-2}	9.5 *($Cl^-_{tolerance}$ = 1400 mg·L^{-1})*	25–380	Q_{net} = 0.0035 CrCOD + 0.056 (R^2 = *0.993)*	49
CE = Pt_{foil}, SE = Na_2SO_4	$I_{UV-light}$ = 20 mW cm^{-2} (230 W)	18.3	20–280	PEC-COD = 0.9326 CrCOD + 3.1576 (R^2 = *0.9801)*	52
WE = TiO_2, CE = Pt_{coil}, SE = Na_2SO_4	I_{light} = 2.0 mW cm^{-2}, E_{bias} = 1.5 V (*vs.* Ag/AgCl)	8 *(2.3 – 5.1% RSD)*	20–250	i_{net} = 3.8458 ThCOD (R^2 = *0.9928, S/N = 3)*	68
WE = TiO_2, CE = Pt_{coil}, SE = Na_2SO_4	I_{light} = 2.0 mW cm^{-2}, E_{bias} = 1.5 V (*vs.* Ag/AgCl)	8 *(2.3 – 5.1% RSD)*	20–250	i_{net} = 3.8458 ThCOD (R^2 = *0.9928, S/N = 3)*	68
WE = 3D Pt-NPs/TNTAs/Ti, SE = Na_2SO_4, Extended-gate field-effect transistor sensor	V_{Cell} = 8.2 µL, $P_{UV-Lamp}$ = 2 W, E_{Bias} = 2.5 V (*vs.* Ag/AgCl)	0.12 *(2.7% RSD)*	1.44–672	i_{net} = 0.0013 log (COD) - 3·10^{-4} (R^2 = *0.9744)*	37
WE = 3D-NPs/TNTAs, SE = Na_2SO_4	E_{bias} = 1.5 V (*vs.* Ag/AgCl), UV illumination	0.18 *(3.7% RSD)*	1.92–3.360	i_{net} = 0.000887 log (COD) – 0.000322 (S/N = 3)	50
CE: Pt	$E_{Amplitude}$ = 10 mV (*vs.* SCE), f = 50 kHz – 0.1 Hz, 10 steps/dec., I_{Light} = 50 W cm^{-2}	0.05	0.20–19.9	Log ($Z_{relative}$) = -0.667 ± 0.012 log (COD) (R^2 = *0.9987, n = 9)*	78
WE = TiO_2, CE = Pt, SE = $NaNO_3$	$d_{UV\ source\ -\ photoanode\ surface}$ = 6.5 mm, I_{Light} = 6.6 mW cm^{-2}, Th $_{film}$ = 2 µm	0.2 (1.5% *RSD*)	1.25–576	i_{net} = 1.063 ThCOD + 0.0953 (R^2 = *0.9967)*	28
WE = CuS/TiO_2/ITO, CE = Pt-NPs, SE = $NaNO_3$	pH 3, t_{assay} = 5 min.	0.017 (ca. 1.5% *RSD*)	0.05–50	V = 0.036 logCOD + 0.438 (R^2 = *0.990)*	55
WE = TiO_2/g-C_3N_4/ITO, RE = Hg/Hg_2Cl_2, CE = Pt	Neutral pH, t_{assay} = 15 min, stability time = 30 min.	0.0084 (ca. 3% *RSD*)	0.025–750	RGB_{blue} = 86.4 COD + 110 *(0.025–0.75 mg L^{-1},* R^2 = *0.934)*, RGB_{blue} = 0.0930 COD + 102 (<*750 mg L^{-1},* R^2 = *0.972)*	54
WE = Te-TiO_2/Ti, CE =Pt, RE = Ag/AgCl.	E_{bias} = 0.6 V (*vs.* Ag/AgCl) at 0.1 mV s^{-1}, 84 compounds tested., UV light source.	<1 µm (ca. 1.8% *RSD*)	1–10 µm	ThCOD = PECOD *(almost 100% accuracy)*	48

WE working electrode, *CE* counter electrode, *SE* supporting electrolyte, *SCE* saturated calomel electrode, *Th* thickness, E_{bias} bias potential, I_{light} light intensity, *V* aliquot volume, t_{assay} assay time, *d* distance between electrodes, *A* electrode area, J_{rate} flow rate, *V* voltage, *Φ* diameter. *RSD* relative standard deviation, *DL* detection limit, *RD* range detection.

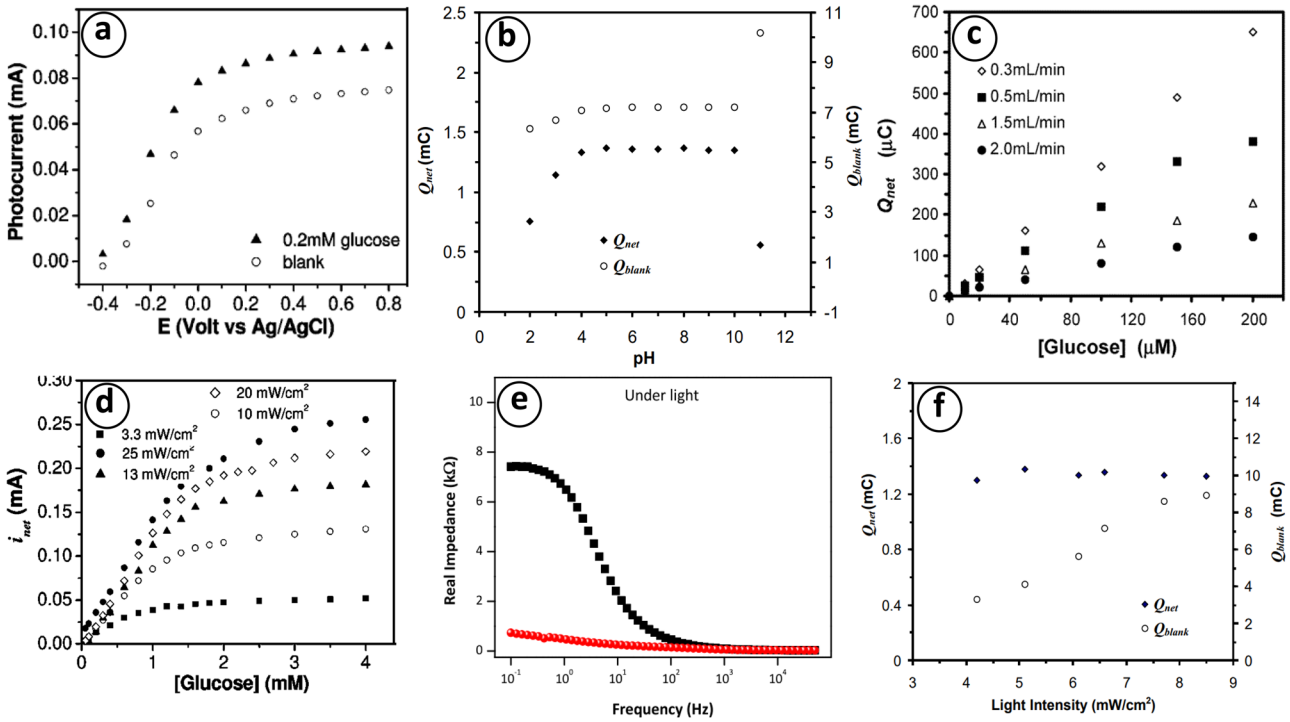

Fig. 7 | Parameter optimization for PEC-COD sensors. a Analyte concentration (Glucose). Adapted from Zhang et al.[72], **b** pH. Adapted from ref. Zhang et al.[44], **c** sample flow rate from ref. Zhang et al.[45], **d** light intensity for different glucose concentrations. Adapted from Zhang et al.[72] **f** light intensity from ref.[44], **e** Impedance under light. Reprinted from Alves et al.[78].

As previously mentioned, Alves et al.[78] investigated the variation in resistance and capacitance of a photoelectrochemiresistive device under visible light during COD quantification, using an EEC (Fig. 6e) with material adsorption. They found that both visible light and the organic charge adsorption added to the photoelectrochemiresistive system decreased the Nyquist semicircle radius in a linear manner; this indicates that light and analytes reduce charge recombination rates, resulting in longer electron-hole separation times and a lower R_{CT} at the vanadate-solution interface[78,95].

Furthermore, the resistance of both charge trapping (R_1) and charge transfer (R_2) depends on the amount of OM; as COD increases, R_2 decreases[78,95], while capacitance is directly proportional to COD and conductivity, which is determined by the phase angle decrease in the Bode plots[78]. Under dark conditions, the semicircles overlap almost completely, signifying that their time constants are approximately equal. The EEC modeling in this scenario consists of two parallel resistance/capacitance (R/CPE) circuits, where R_1 and CPE_1 represent the R_{CT} and double-layer capacitance, respectively, while CPE_2/R_2 is attributed to the porosity of $BiVO_4$ over FTO ($R_1 CPE_1 / R_2 CPE_2 \approx 1$) [78,95]. At 63 Hz, the phase angle is constant for all COD concentrations, indicating no significant relationship between R_{CT} and COD, implying that R_{CT} is limited by $BiVO_4$ active sites in absence of light[78].

Conclusions and future perspectives

The development of PC-COD sensors and PEC-COD sensors involves facing and overcoming several challenges, including portability, low cost, easy automation, sensitivity, rapid detection, on-site detection, and fast response time. These challenges encompass analytical, instrumental, environmental, and economic aspects. For PEC-COD sensors, overcoming these challenges primarily depends on the optical, mechanical, and electrical properties of the electrode used.

This review examined that, the morphological and structural control of nanomaterials, through different synthetic pathways and modifications, influences the efficiency of PC activity in PC-COD and PEC-COD sensors. Fabricating mono- and heterostructured nanomaterials has demonstrated the ability to enhance the signal of quantification, stability, conductivity, and reproducibility, as well as optimize particle size, contact area, oxygen vacancy generation, surface hydrogenation, and doping levels. These improvements help overcome the limitations of charge separation mechanisms. The performance of PEC-COD sensors—including sensitivity, detection limits, reproducibility, stability, accuracy, and precision—depends on the material used in the working electrode, as well as on operating variables such as applied polarization current or potential, reactor type, light intensity and pH, which significantly influence the sensor's effectiveness and reproducibility.

Over 80% of nanomaterials that have been utilized in PC-COD and PEC-COD sensors to date are based on titanium dioxide. Below, we detail a series of semiconductors that have demonstrated excellent experimental and theoretical performance in PEC oxidations. These materials have shown advancements in the design and engineering of crystallinity and heterojunction, making them suitable for COD sensors with catalytic activity under visible light, thereby guiding future research development. The recommended PC materials contrast with several characteristics and properties emphasized in this review, include:

- Bi-based nanomaterials, such as oxyhalides ($BiOX; X = F, Cl, Br, I$), molybdates (e.g., Bi_2MoO_6), wolframite (e.g., Bi_2WO_6), and vanadates (e.g., $BiVO_4$), are potentially used in PEC systems, where in overall their stable structural arrangement, low toxicity, and narrow band gap make them ideal for the separation and transport of photogenerated charges, even in heterostructured systems they improve the stability and final conductivity of the electrodes.
- Metal-organic frameworks (MOFs)—Structurally bulky and porous, they are typically metals coordinated or sub-coordinated with heteroatoms from organic ligands. Becomes interesting for these applications due to their high surface area, which allows for the efficient detection and quantification of organic compounds. Further, their structural versatility enables, for instance, the metal incorporations or the hybrid formations with semiconductors, enhancing their PC activity, stability, and conductivity.
- Piezoelectric, pyroelectric, and single-phase magnetic materials, such as mixed magnetic oxides like cobalt ferrite doped with binary titanium or

niobium oxide, as well as those based on perovskites. These materials possess mechanical, thermal, electrical, and magnetic properties that are highly advantageous, enhancing the performance of PEC processes and sensors. The synergy of these characteristics would optimize the charge distribution, detection time, reproducibility, and stability of the system.

It is important to consider that the continuous attempts to miniaturize various processes at the nanoscale level have led to nanoscience being regarded as one of the most important areas of scientific study nowadays. These processes include the development of materials and devices such as optoelectronics, sensing, driven molecules, and catalysts. In order to use nanomaterials as selective and effective homogeneous and heterogeneous (photo)catalysts, scientists, including chemists and engineers, have been working closely together thanks to the advancements in nanoscience. This has led to a meteoric rise in the popularity of catalysis involving COD sensors over the past few years.

This review draws the reader in by combining fundamental theoretical concepts with plenty of relevant examples. The area of sensors by photocatalysts with nanoparticles is currently growing, and it is expected that important obstacles will soon be overcome, leading to nanoparticle catalysis finding many more uses. Therefore, this review will be great impact in academic and industrial fields in the chemical sciences.

Received: 1 October 2024; Accepted: 29 November 2024;
Published online: 19 December 2024

References

1. dos Santos, A. J. et al. Accelerating innovative water treatment in Latin America. *Nat. Sustain.* **2023**, 1–3, https://doi.org/10.1038/s41893-022-01042-z (2023).
2. Li, J., Luo, G., He, L. J., Xu, J. & Lyu, J. Analytical approaches for determining chemical oxygen demand in water bodies: a review. 10.1080/10408347.2017.1370670 48, 47–65 (2017).
3. Geerdink, R. B., Sebastiaan van den Hurk, R. & Epema, O. J. Chemical oxygen demand: historical perspectives and future challenges. *Anal. Chim. Acta* **961**, 1–11 (2017).
4. da Silva, J. C. O. et al. Achieving sustainable development goal 6 electrochemical-based solution for treating groundwater polluted by fuel station. *Water* **14**, 2911 (2022).
5. Espinoza-Montero, P. J., Martínez-Huitle, C. A. & Loor-Urgilés, L. D. Technologies employed for carwash wastewater recovery. *J. Clean. Prod.* **401**, 136722 (2023).
6. Alipour, Z. & Azari, A. COD removal from industrial spent caustic wastewater: a review. *J. Environ. Chem. Eng.* **8**, 103678 (2020).
7. Rodrigo, M. A., Oturan, M. A. & Oturan, N. Electrochemically assisted remediation of pesticides in soils and water: a review. *Chem. Rev.* **114**, 8720–8745 (2014).
8. Brillas, E. & Martínez-Huitle, C. A. Decontamination of wastewaters containing synthetic organic dyes by electrochemical methods. An updated review. *Appl. Catal. B* **166–167**, 603–643 (2015).
9. Eniola, J. O., Kumar, R., Barakat, M. A. & Rashid, J. A review on conventional and advanced hybrid technologies for pharmaceutical wastewater treatment. *J. Clean. Prod.* **356**, 131826 (2022).
10. Narayan Thorat, B. & Kumar Sonwani, R. Current technologies and future perspectives for the treatment of complex petroleum refinery wastewater: a review. *Bioresour. Technol.* **355**, 127263 (2022).
11. Ochoa-Chavez, S. A., Montenegro-Rosero, K. L., Espinoza-Montero, P. J., Yar-Hernández, A. V. & Frontana-Uribe, B. A. Advanced oxidation processes for removal of pharmaceuticals and personal care products. *Development in Wastewater Treatment Research and Processes: Emerging Technologies for Removal of Pharmaceuticals and Personal Care Products: State of the Art, Challenges and Future Perspectives* 255–286 (2024) https://doi.org/10.1016/B978-0-443-19207-4.00014-8.
12. Martínez-Huitle, C. A., Rodrigo, M. A., Sirés, I. & Scialdone, O. A critical review on latest innovations and future challenges of electrochemical technology for the abatement of organics in water. *Appl Catal. B* **328**, 122430 (2023).
13. de Castro, C. M. et al. Environmental application of a cost-effective smartphone-based method for COD analysis: Applicability in the electrochemical treatment of real wastewater. *Sci. Total Environ.* **855**, 158816 (2023).
14. Ma, J. Determination of chemical oxygen demand in aqueous samples with non-electrochemical methods. *Trends Environ. Anal. Chem.* **14**, 37–43 (2017).
15. Li, L., Zhang, S., Li, G. & Zhao, H. Determination of chemical oxygen demand of nitrogenous organic compounds in wastewater using synergetic photoelectrocatalytic oxidation effect at TiO2 nanostructured electrode. *Anal. Chim. Acta* **754**, 47–53 (2012).
16. Zhu, L., Chen, Y., Wu, Y., Li, X. & Tang, H. A surface-fluorinated-TiO2-KMnO4 photocatalytic system for determination of chemical oxygen demand. *Anal. Chim. Acta* **571**, 242–247 (2006).
17. Chen, H. et al. Assessment of a COD analytical method based on the photoelectrocatalysis of a TiO_2 nanotube array sensor. *Anal. Methods* **4**, 1790–1796 (2012).
18. Carchi, T. et al. A Nafion film cover to enhance the analytical performance of the CuO/Cu electrochemical sensor for determination of chemical oxygen demand. *Sensors* **19**, 669 (2019).
19. Ai, S. et al. Study on photocatalytic oxidation for determination of chemical oxygen demand using a nano-TiO_2-$K_2Cr_2O_7$ system. *Anal. Chim. Acta* **509**, 237–241 (2004).
20. Zhang, Z. et al. Preparation of photocatalytic nano-ZnO/TiO_2 film and application for determination of chemical oxygen demand. *Talanta* **73**, 523–528 (2007).
21. Chai, Y. et al. Study on photocatalytic oxidation for determination of the low chemical oxygen demand using a nano-TiO_2-$Ce(SO_4)_2$ coexisted system. *Talanta* **68**, 610–615 (2006).
22. Boczkaj, G. & Fernandes, A. Wastewater treatment by means of advanced oxidation processes at basic pH conditions: a review. *Chem. Eng. J.* **320**, 608–633 (2017).
23. Oturan, M. A. & Aaron, J. J. Advanced oxidation processes in water/wastewater treatment: principles and applications. a review. *Crit. Rev. Environ. Sci. Technol.* **44**, 2577–2641 (2014).
24. Byrne, C., Subramanian, G. & Pillai, S. C. Recent advances in photocatalysis for environmental applications. *J. Environ. Chem. Eng.* **6**, 3531–3555 (2018).
25. Ganiyu, S. O. & Martínez-Huitle, C. A. The use of renewable energies driving electrochemical technologies for environmental applications. *Curr. Opin. Electrochem* **22**, 211–220 (2020).
26. Ganiyu, S. O., Martínez-Huitle, C. A. & Rodrigo, M. A. Renewable energies driven electrochemical wastewater/soil decontamination technologies: A critical review of fundamental concepts and applications. *Appl Catal. B* **270**, 118857 (2020).
27. Aghasadeghi, K., Larocque, M. J. & Latulippe, D. R. Towards the real-time monitoring of industrial wastewater treatment processes: via photoelectrochemical oxygen demand measurements. *Environ. Sci.* **4**, 394–402 (2018).
28. Zu, M. et al. Designing robust anatase-branch@hydrogenated-rutile-nanorod TiO_2 as accurate and sensitive photoelectrochemical sensors. *Sens. Actuators B Chem.* **321**, 128504 (2020).
29. Pang, Y. et al. Synthesis of α-$Bi_2Mo_3O_{12}$/TiO_2 nanotube arrays for photoelectrochemical COD detection application. *Langmuir* **33**, 8933–8942 (2017).
30. Natividad, R., Barrera-Díaz, C., Martínez-Huitle, C. A. & Rodríguez-Rodríguez, J. M. Towards sustainability: photochemical and electrochemical processes applied for environmental protection. *Int. J. Photoenergy* **2018**, 1–3 (2018).

31. Oturan, M. A. Electrochemical advanced oxidation technologies for removal of organic pollutants from water. *Environ. Sci. Pollut. Res.* **21**, 8333–8335 (2014).
32. Moreira, F. C., Boaventura, R. A. R., Brillas, E. & Vilar, V. J. P. Electrochemical advanced oxidation processes: a review on their application to synthetic and real wastewaters. *Appl Catal. B* **202**, 217–261 (2017).
33. Sirés, I., Brillas, E., Oturan, M. A., Rodrigo, M. A. & Panizza, M. Electrochemical advanced oxidation processes: today and tomorrow. A review. *Environ. Sci. Pollut. Res.* **21**, 8336–8367 (2014).
34. Vasudevan, S. & Oturan, M. A. Electrochemistry: as cause and cure in water pollution-an overview. *Environ. Chem. Lett.* **12**, 97–108 (2014).
35. Bessegato, G. G., Guaraldo, T. T., de Brito, J. F., Brugnera, M. F. & Zanoni, M. V. B. Achievements and trends in photoelectrocatalysis: from environmental to energy applications. *Electrocatalysis* **6**, 415–441 (2015).
36. Kusmierek, E. Semiconductor Electrode Materials Applied in Photoelectrocatalytic Wastewater Treatment-an Overview. *Catalysts* **10**, 439 (2020).
37. Si, H. et al. A real-time on-line photoelectrochemical sensor toward chemical oxygen demand determination based on field-effect transistor using an extended gate with 3D TiO_2 nanotube arrays. *Sens. Actuators B Chem.* **289**, 106–113 (2019).
38. Bakan, B. et al. Circular economy applied to organic residues and wastewater: research challenges. *Waste Biomass Valoriz.* **13**, 1267–1276 (2022).
39. Mu, Q., Li, Y., Zhang, Q. & Wang, H. TiO_2 nanofibers fixed in a microfluidic device for rapid determination of chemical oxygen demand via photoelectrocatalysis. *Sens. Actuators B Chem.* **155**, 804–809 (2011).
40. Yuan, S., Mao, R., Li, Y., Zhang, Q. & Wang, H. Layer-by-layer assembling TiO_2 film from anatase TiO_2 sols as the photoelectrochemical sensor for the determination of chemical oxygen demand. *Electrochim. Acta* **60**, 347–353 (2012).
41. Li, S. et al. Photoelectrochemical characterization of hydrogenated TiO_2 nanotubes as photoanodes for sensing applications. *ACS Appl. Mater. Interfaces* **5**, 11129–11135 (2013).
42. Wang, X. et al. Visible light photoelectrochemical properties of a hydrogenated TiO_2 nanorod film and its application in the detection of chemical oxygen demand. *RSC Adv.* **5**, 76315–76320 (2015).
43. Han, Y. et al. Robust TiO_2/BDD heterojunction photoanodes for determination of chemical oxygen demand in wastewaters. *Anal. Methods* **3**, 2003–2009 (2011).
44. Zhang, S., Zhao, H., Jiang, D. & John, R. Photoelectrochemical determination of chemical oxygen demand based on an exhaustive degradation model in a thin-layer cell. *Undefined* **514**, 89–97 (2004).
45. Zhang, S., Jiang, D. & Zhao, H. Development of chemical oxygen demand on-line monitoring system based on a photoelectrochemical degradation principle. *Environ. Sci. Technol.* **40**, 2363–2368 (2006).
46. Li, J. et al. Determination of chemical oxygen demand using flow injection with Ti/TiO_2 electrode prepared by laser anneal. *Meas. Sci. Technol.* **18**, 945–951 (2007).
47. Zheng, Q. et al. Self-organized TiO_2 nanotube array sensor for the determination of chemical oxygen demand. *Adv. Mater.* **20**, 1044–1049 (2008).
48. Nurdin, M. et al. Enhanced photoelectrocatalytic performance using chalcogenide Te/TiO_2/Ti nanotube array based on COD analyses for water treatment applications. *Electrocatalysis* **14**, 581–592 (2023).
49. Qu, X., Tian, M., Chen, S., Liao, B. & Chen, A. Determination of chemical oxygen demand based on novel photoelectro-bifunctional electrodes. *Electroanalysis* **23**, 1267–1275 (2011).
50. Si, H., Zhang, X. & Lin, S. A simple flow injection sensing system for the real-time on-line determination of chemical oxygen demand based on 3D Au-NPs/TiO_2 nanotube arrays. *Front. Mater.* **6**, 238 (2019).
51. Liang, L. et al. Preparation of Au nanoparticles modified TiO_2 nanotube array sensor and its application as chemical oxygen demand sensor. *Chin. Chem. Lett.* **30**, 167–170 (2019).
52. Wang, C. et al. Photoelectrocatalytic determination of chemical oxygen demand under visible light using Cu_2O-loaded TiO_2 nanotube arrays electrode. *Sens. Actuators B Chem.* **181**, 1–8 (2013).
53. Wang, C. et al. Investigation on the application of titania nanorod arrays to the determination of chemical oxygen demand. *Anal. Chim. Acta* **767**, 141–147 (2013).
54. Dai, Z. et al. Portable photoelectrochromic visualization sensor for detection of chemical oxygen demand. *Anal. Chem.* **92**, 13604–13609 (2020).
55. Hao, N. et al. Rapid potentiometric detection of chemical oxygen demand using a portable self-powered sensor chip. *Anal. Chem.* **93**, 8393–8398 (2021).
56. Bai, S., Zhang, N., Gao, C. & Xiong, Y. Defect engineering in photocatalytic materials. *Nano Energy* **53**, 296–336 (2018).
57. Sun, X., Wang, C., Su, D., Wang, G. & Zhong, Y. Application of photocatalytic materials in sensors. *Adv. Mater. Technol.* **5**, 1900993 (2020).
58. Castillo-Cabrera, G. X. & Espinoza-Montero, P. J. Novel trends in mixed oxide electrodes for photoelectrocatalytic wastewater treatment. *Curr. Opin. Electrochem.* **44**, 101448 (2024).
59. Quilumbaquin, W., Castillo-Cabrera, G. X., Borrero-González, L. J. & Espinoza-Montero, P. J. Protocol for the preparation of TiO2-modified boron-doped diamond photoelectrode via electrophoretic deposition and its photoelectrochemical study. *STAR Protoc.* **5**, 103259 (2024).
60. Alulema-Pullupaxi, P. et al. Fundamentals and applications of photoelectrocatalysis as an efficient process to remove pollutants from water: a review. *Chemosphere* **281**, 130821 (2021).
61. Espinoza-Montero, P. J., Vargas, R., Alulema-Pullupaxi, P. & Fernández, L. Photoelectrocatalysis: Principles and Applications. *Advanced Oxidation Processes for Wastewater Treatment* 53–68 (2022) https://doi.org/10.1201/9781003165958-5.
62. Ikram, M. et al. A review of photocatalytic characterization, and environmental cleaning, of metal oxide nanostructured materials. *Sustain. Mater. Technol.* **30**, e00343 (2021).
63. Wang, Z., Lin, Z., Shen, S., Zhong, W. & Cao, S. Advances in designing heterojunction photocatalytic materials. *Chin. J. Catal.* **42**, 710–730 (2021).
64. Tong, H. et al. Nano-photocatalytic materials: possibilities and challenges. *Adv. Mater.* **24**, 229–251 (2012).
65. Imai-Imada, M. et al. Orbital-resolved visualization of single-molecule photocurrent channels. *Nature* **603**, 829–834 (2022). *2022 603:7903*.
66. Quilumbaquin, W. et al. Photoelectrocatalytic degradation of high-density polyethylene microplastics on TiO2-modified boron-doped diamond photoanode. *iScience* **27**, 109192 (2024).
67. Wu, H. et al. Photocatalytic and photoelectrochemical systems: similarities and differences. *Adv. Mater.* **32**, 1904717 (2020).
68. Zhang, Z., Chang, X. & Chen, A. Determination of chemical oxygen demand based on photoelectrocatalysis of nanoporous TiO_2 electrodes. *Sens. Actuators B Chem.* **223**, 664–670 (2016).
69. Bai, J. & Zhou, B. Titanium dioxide nanomaterials for sensor applications. *Chem. Rev.* **114**, 10131–10176 (2014).
70. Bai, S., Gao, C., Low, J. & Xiong, Y. Crystal phase engineering on photocatalytic materials for energy and environmental applications. *Nano Res.* **12**, 2031–2054 (2019).
71. Silva, C. R., Conceição, C. D. C., Bonifácio, V. G., Filho, O. F. & Teixeira, M. F. S. Determination of the chemical oxygen demand (COD) using a copper electrode: a clean alternative method. *J. Solid State Electrochem.* **13**, 665–669 (2009).
72. Zhang, S., Li, L. & Zhao, H. A portable photoelectrochemical probe for rapid determination of chemical oxygen demand in wastewaters. *Environ. Sci. Technol.* **43**, 7810–7815 (2009).

73. Cheng, Q., Wu, C., Chen, J., Zhou, Y. & Wu, K. Electrochemical tuning the activity of nickel nanoparticle and application in sensitive detection of chemical oxygen demand. *J. Phys. Chem. C.* **115**, 22845–22850 (2011).
74. Zhang, J. et al. Photoelectrocatalytic COD determination method using highly ordered TiO_2 nanotube array. *Water Res* **43**, 1986–1992 (2009).
75. Hu, Y. S., Zhao, Y. Q. & Sorohan, B. Removal of glyphosate from aqueous environment by adsorption using water industrial residual. *Desalination* **271**, 150–156 (2011).
76. Materials Data on TiO_2 by Materials Project. https://doi.org/10.17188/1207597 (2020).
77. Liao, J., Lin, S., Zeng, M. & Yang, Y. A miniature photoelectrochemical sensor based on organic electrochemical transistor for sensitive determination of chemical oxygen demand in wastewaters. *Water Res.* **94**, 296–304 (2016).
78. Alves, N. A., Olean-Oliveira, A., Cardoso, C. X. & Teixeira, M. F. S. Photochemiresistor sensor development based on a bismuth vanadate type semiconductor for determination of chemical oxygen demand. *ACS Appl. Mater. Interfaces* **12**, 18723–18729 (2020).
79. Xiong, J., Song, P., Di, J., Li, H. & Liu, Z. Freestanding ultrathin bismuth-based materials for diversified photocatalytic applications. *J. Mater. Chem. A Mater.* **7**, 25203–25226 (2019).
80. Kumar, R. et al. An overview on bismuth molybdate based photocatalytic systems: controlled morphology and enhancement strategies for photocatalytic water purification. *J. Environ. Chem. Eng.* **8**, 104291 (2020).
81. Naciri, Y. et al. Recent progress on the enhancement of photocatalytic properties of BiPO4 using π–conjugated materials. *Adv. Colloid Interface Sci.* **280**, 102160 (2020).
82. Ding, K., Chen, B., Li, Y., Zhang, Y. & Chen, Z. Comparative density functional theory study on the electronic and optical properties of $BiMO_4$ (M = V, Nb, Ta). *J. Mater. Chem. A Mater.* **2**, 8294–8303 (2014).
83. Sánchez-Montes, I. et al. Assessing the performance of electrochemical oxidation using DSA® and BDD anodes in the presence of UVC light. *Chemosphere* **238**, 124575 (2020).
84. Yu, H., Wang, H., Quan, X., Chen, S. & Zhang, Y. Amperometric determination of chemical oxygen demand using boron-doped diamond (BDD) sensor. *Electrochem. Commun.* **9**, 2280–2285 (2007).
85. Ding, M., Liu, Y., Lu, X., Li, Y. & Tang, W. Boron doped diamond films: a microwave attenuation material with high thermal conductivity. *Appl. Phys. Lett.* **114**, 162901 (2019).
86. de Freitas Araújo, K. C., da Silva, D. R., dos Santos, E. V., Varela, H. & Martínez-Huitle, C. A. Investigation of persulfate production on BDD anode by understanding the impact of water concentration. *J. Electroanal. Chem.* **860**, 113927 (2020).
87. Garcia-Segura, S., Vieira Dos Santos, E. & Martínez-Huitle, C. A. Role of sp3/sp2 ratio on the electrocatalytic properties of boron-doped diamond electrodes: a mini review. *Electrochem. Commun.* **59**, 52–55 (2015).
88. Martínez-Huitle, C. A., Ferro, S. & De Battisti, A. Electrochemical incineration in the presence of halides. *Electrochem. Solid-State Lett.* **8**, D35 (2005).
89. Ganiyu, S. O., dos Santos, E. V., Martínez-Huitle, C. A. & Waldvogel, S. R. Opportunities and challenges of thin-film boron-doped diamond electrochemistry for valuable resources recovery from waste: organic, inorganic, and volatile product electrosynthesis. *Curr. Opin. Electrochem.* **32**, 100903 (2022).
90. Zhao, H., Jiang, D., Zhang, S., Catterall, K. & John, R. Development of a direct photoelectrochemical method for determination of chemical oxygen demand. *Anal. Chem.* **76**, 155–160 (2003).
91. Zhao, H., Jiang, D., Zhang, S., Catterall, K. & John, R. Development of a direct photoelectrochemical method for determination of chemical oxygen demand. *Anal. Chem.* **76**, 155–160 (2004).
92. Araújo, K. C., dos Santos, E. V., Nidheesh, P. V. & Martínez-Huitle, C. A. Fundamentals and advances on the mechanisms of electrochemical generation of persulfate and sulfate radicals in aqueous medium. *Curr. Opin. Chem. Eng.* **38**, 100870 (2022).
93. Ganiyu, S. O., Martínez-Huitle, C. A. & Oturan, M. A. Electrochemical advanced oxidation processes for wastewater treatment: advances in formation and detection of reactive species and mechanisms. *Curr. Opin. Electrochem.* **27**, 100678 (2021).
94. Zhang, S., Li, L., Zhao, H. & Li, G. A portable miniature UV-LED-based photoelectrochemical system for determination of chemical oxygen demand in wastewater. *Sens. Actuators B Chem.* **141**, 634–640 (2009).
95. Brett, C. M. A. Electrochemical impedance spectroscopy in the characterisation and application of modified electrodes for electrochemical sensors and biosensors. *Molecules* **27**, 1497 (2022).
96. Li, J., Li, L., Zheng, L., Xian, Y. & Jin, L. Rh_2O_3/Ti electrode preparation using laser anneal and its application to the determination of chemical oxygen demand. *Meas. Sci. Technol.* **17**, 1995–2000 (2006).

Acknowledgements

Financial support from Pontificia Universidad Católica del Ecuador, Project code: QINV0402-IINV529020100. Financial support from Fundação Coordenação de Aperfeiçoamento de Pessoal de Nível Superior (CAPES, Brazil), as Master fellowships, are gratefully acknowledged.

Author contributions

Conceived the project, E.-M.P.J. and L.-U.L.D., and M.-H.C.A.; visualization, L.-U.L.D. and E.-M.P.J.; supervision, E.-M.P.J.; investigation, L.-U.L.D., F.TN., M.-H.C.A., V.S.E., and E.-M.P.J.; writing—original draft preparation, L.-U.L.D., F.TN., M.-H.C.A., V.S.E., and E.-M.P.J.; writing—review and editing, L.-U.L.D., F.TN., M.-H.C.A., V.S.E., and E.-M.P.J.; project administration, P.J.E.-M. and M.-H.C.A.; funding acquisition, P. J.E.-M. and M.-H.C.A. All authors have read and agreed to the published version of the manuscript.

Competing interests

The authors declare no competing interests.

Additional information

Correspondence and requests for materials should be addressed to Patricio J. Espinoza-Montero.